Siegfried Zöhrer, BSc

Xylan Adsorption on Thin Cellulose Model Films

MASTER THESIS

For obtaining the academic degree
Diplom-Ingenieur

Master Programme of
Technical Physics

Graz University of Technology

Supervisor:
Ao.Univ.-Prof. Mag. Dr.rer.nat Robert Schennach
Institute of Solid State Physics

Graz, May 2014

Statutory declaration

I declare that I have authored this thesis independently, that I have not used other than the declared sources/resources, and that I have explicitly indicated all material which has been quoted either literally or by content from the sources used. The text document uploaded to TUGRAZonline is identical to the present master's thesis.

Graz, _____ _____

Date Signature

Eidesstaatliche Erklärung

Ich erkläre an Eides statt, dass ich die vorliegende Arbeit selbstständig verfasst, andere als die angegebenen Quellen/Hilfsmittel nicht benutzt, und die den benutzten Quellen wörtlich und inhaltlich entnommenen Stellen als solche kenntlich gemacht habe. Das in TUGRAZonline hochgeladene Textdokument ist mit der vorliegenden Masterarbeit identisch.

Graz, am _____ _____

Datum Unterschrift

Abstract

When investigating a complex material like cellulose, a simplified model system can be crucial. In this work, a recently developed model of thin cellulose films on silicon substrates was used to conduct three experiments about fundamental cellulose properties with industry interest. The first one tries to examine the bonding mechanism of cellulose model films using infrared spectroscopy. Water swelling and drying is used to establish bonds between two films. Then, the bound films were compared to unbound ones by polarisation modulation Fourier-transform infrared spectroscopy. The second experiment analyses xylan adsorption on a cellulose surface from an aqueous xylan electrolyte. Quartz microbalance with dissipation was used to investigate this adsorption process qualitatively and to estimate the amount of xylan adsorbed. The last experiment concerns the interaction of two xylan adsorbed cellulose surfaces. The tensile force required to separate pairs of those films, which were bound by swelling and drying in water, was measured. The results showed unexpected high forces compared to the findings in literature with pure cellulose and spin-coated xylan samples. Moreover, the experiment emphasised the vital role of ionic compounds in these surface interactions. All three experiments are based on the same model films, the same resources and similar adsorption processes. Therefore, they are comparable and can be discussed in combination. This thesis was embedded in the recent research at the “Christian Doppler Laboratory for Surface Chemical and Physical Fundamentals of Paper Strength”.

Contents

1 Introduction

The organic material cellulose has always had countless applications. Since humans started to utilise wood, they made use out of cellulose because 40 to 47% of wood is made of it [29, p. 2]. In fact, most plants have a high cellulose content. Many macroscopic physical properties of cellulose based products like paper and textile fabrics (cotton consists of 95% cellulose [29, p. 2]) are related to the microscopical structure of these molecules. In the historical process of advancing those applications, an interest of the underlying molecular structure evolved naturally.

The first documented scientific approach to extract and analyse cellulose was done by the French chemist Anselme Payem in 1838 [13, p. 3358]. His analysis lead to the assumption that there is a common chemical species in several tested plant tissues with a certain ratio of carbon, oxygen and hydrogen ($C_6H_{10}O_5$) [29, p. 7]. Several important developments in cellulose chemistry followed in this century. For example the synthesis of cellulose nitrate, which lead to new industrial applications like thermoplastic materials or "artificial silk" [12, p. 3]. As cellulose is insoluble in most common solvents, another example of a major advance is the first discovery of a capable solvent, a cuprammonium hydroxide solution in 1857 [12, p. 2].

However, the most important discovery concerning cellulose structure, followed in the early 20^{th} century. In 1920, the German chemist Hermann Staudinger realised that cellulose consists out of long molecular chains and laid the foundation of polymer science [13, p. 3360]. From this point on, improving imaging techniques like x-ray diffraction, infrared & Raman spectroscopy, nuclear magnetic resonance and others, lead to continuous advances in understanding the

molecular and supramolecular structure of cellulose which is still an ongoing process.

1.1 Cellulose structure

The cellulose molecule is built up of glucose. To be more exact, β-D-glucopyranose which is shown in figure 1.1 in chair conformation [13, p. 3360]. This molecule forms a ring out of five carbon atoms and one oxygen atom (pyranose) which is coloured blue in the figure. Chair conformation means, that the pyranose ring is not strictly planar, which accommodates the favoured bonding angles. The letter D stands for one of the two glucose enantiomeres (mirror images, the other one is L) and β denotes the orientation of the hydroxy group (OH) at the first carbon atom in respect to the ring plane (coloured red in figure 1.1). The carbon atoms are usually numbered from one to six and referred to as C1 to C6. [4, chp. 22]

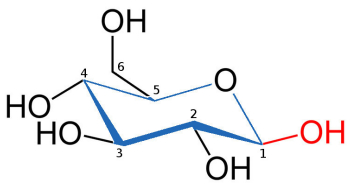

Figure 1.1: The β-D-gluco-pyranose molecule ($C_6H_{12}O_6$).

These glucose molecules form covalent bonds between each other at the OH group at C4 and the carbon atom C1 (β-1,4-glycosidic bond) which results in a molecular chain. Every second segment is rotated by 180° in plane because of favoured bonding angles [13, p. 3360]. The resulting polymer is shown in figure 1.2, where $n \in \{5, 6, 7, \dots\}$ β-D-glucopyranose units are bound in this way. The degree of polymerization (DP) in this representation is $n > 4$. To give an example, the average DP of cellulose in wood (various species) lies between 6000 and 10000 [29, p. 4]. At the ends of the molecular chain, instead of the glycosidic bond, an OH-group is attached to C4 (reducing end) and a CHO-group to C1 (non-reducing end) [12, p. 10].

A very important factor of this chemical structure are the three hydroxy groups per unit. Dipole-dipole interactions between them result in intra- and intermolecular bonds (hydrogen bonds) which leads to stiffer chains and a supramolecular

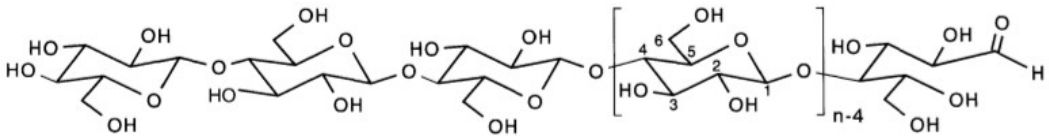

Figure 1.2: Molecular structure of the polymer cellulose $(C_6H_{10}O_5)_n$ [12, p. 10].

cellulose structure. Because of the specific positions and orientations of these hydroxy groups, cellulose shows both - crystalline and amorphous areas in solid state. In the crystalline parts of native cellulose (type I), the chains align parallel and two different crystal structures appear in combination. The first one has a triclinic unit cell with one chain in it (cellulose I_α) and the second has a monoclinic unit cell with two chains in it (cellulose I_β) [13, p. 3362]. The triclinc lattice has the lowest symmetry of all fourteen three dimensional Bravais cells. If provided enough energy (heat treatment), cellulose I_α can irreversibly transition to the higher ordered monoclinic lattice ($I_\alpha \rightarrow I_\beta$) [29, p. 102]. Furthermore, cellulose I alters its structure when it is solved and recrystallised. The glucose conformation is modified [15, p. 4546] and antiparallel chains are formed. This leads to a monoclinic lattice with different hydrogen bonds compared to type I_β. For example, such a transition can be achieved by treating type I cellulose with 20% aqueous sodium hydroxide solution, washing and drying (mercerization) [29, p. 103]. The resulting structure is called cellulose II and "is the most stable structure of technical relevance" [13, p. 3362]. There are more structures of cellulose, in particular type III, IV or the unordered regions (amorphous) which will not be discussed here. In general. the topic is still subject of current research. For example, the conversion from parallel to antiparallel chain alignment and the explanation why type I is preferred in nature are not fully understood [13, p. 3363].

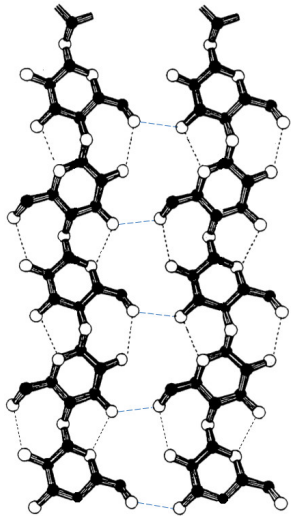

Figure 1.3: Most probable intra- and intermolecular hydrogen bonds in cellulose I [12, p. 14].

Another important factor of cellulose structure is fibril formation. Cellulose crystallites arrange into microfibrils with lateral dimensions in the nanometer region. The size of the crystallites, the amorphous areas in these microfibrils and the cross section varies per cellulose species and morphology. In native cellulose, the crystallites are usually smaller than 20 nm. In cellulose II, the crystallite dimension is 4 to 5 nm and independent of the raw material. In plants, cellulose microfibrils are bundled, combined with xylan, lignin and pectin and form hierarchical structures, which account for most of the macroscopic properties. [13, p. 3364]

1.2 Xylan

Instead of glucose, the basis of a xylan molecule is a chain of xylose units which leads to a different supramolecular structure compared to cellulose. An important difference are branches. Xylan polymers have a main chain consisting out of one molecule (homopolymer) with a DP of 50 to 200. But they also show side branches at irregular intervals, including other molecules and functional groups. A consequence of the branches (side chains) is that xylans do not show a crystalline structure – they are amorphous. Figure 1.4 shows an example of a xylan molecule. One side branch is indicated, a 4-O-methylglucuronic acid, furthermore, several OH groups are substituted by O-acetyl groups. This composition is usually found in hardwoods. [27, pp. 28–29]

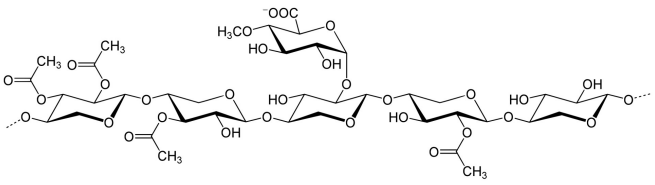

Figure 1.4: Hardwood xylan, showing the main xylose chain, a 4-O-methylglucuronic acid side branch and four O-acetyl groups (substituted OH groups).

1.3 The model system

Since cellulose is a complex material, it is beneficial to create a simplified model system, where properties like the influence of macroscopic structures can be neglected. In the last two decades, a practical approach to further examine the fundamentals of this material evolved. Namely, the deposition of thin cellulose model films on a substrate. The first preparation of such cellulose model films was reported by Schaub et al. [25] in 1993. The cellulose derivate trimethylsilyl cellulose (TMSC) was used to create ultra thin cellulose films on silicon substrates using Langmuir–Blodgett (LB) deposition. In the next years it turned out, that spincoating leads to films in similar quality, but with the advantages of high reproducibility and fast preparation [16, p. 1292]. It was introduced in this field by Geffroy et al. [8] in 1999 and refined into a "novel method preparing cellulose films by spin coating" by Kontturi et al. [17] in 2003. Using such model films, adsorption on cellulose surfaces, the swelling behaviour, or interactions between cellulose surfaces can be examined in a controlled and reproducible fashion. In the last years, this approach has led to several small steps in the route to a clearer picture of cellulose and its properties.

1.4 Bonding mechanism

For cellulose fibre-fibre bonds, a model featuring five different bonding mechanisms was suggested in 2005 by Lindström et al. [18]. These bonding mechanisms are Coulomb interactions, Van der Waals interactions, hydrogen bonding, interdiffusion and mechanical interlocking [18, pp. 476–479]. All of them contribute to the bonding strength of cellulose fibre surfaces – their energy distribution is a current research topic. Some of them require direct molecular contact of the surfaces - especially hydrogen bonding. In contrast to that, mechanical interlocking requires a rough surface (low molecular contact) per definition. Cellulose model films have very smooth surfaces and mechanical interlocking can be neglected. The molecules which diffuse between the surfaces (interdiffusion) also show Coulomb and Van der Waals interactions and possibly hydrogen

bonding. As a result, those three bonding types are most relevant in cellulose model films [22, p. 6].

1.5 The experiments and their motive

An important driving force in this research area is the industry. Especially companies with a focus on paper are interested in a better understanding of adsorption, interaction and swelling behaviour regarding cellulose surfaces. For example in paper fabrication, polyelectrolytes are adsorbed on paper to improve the quality of the product [16, p. 1294]. Another example is the adsorption of dyes on cloth and paper (printing). Also the interaction of cellulose surfaces is an important factor in paper industry. Fundamental information on bonding mechanisms between cellulose or hemi-cellulose (e. g. xylan) surfaces could help to improve paper design to achieve e. g. higher tensile strength in the product. Furthermore, the swelling behaviour of cellulose fibres in aqueous media is of interest in the paper recycling process. [16, p. 1294]. To gain further insight in those areas, experimental research is inevitable. The motive of this work is a contribution to this process.

The bonding between cellulose fibres is a popular research field with many open questions. Cellulose model films are amorphous and show no fibre structure. Still, the bonding process of model films through swelling and drying can give insights on a fundamental level. An important bonding mechanism can be neglected (mechanical interlocking) which makes it easier to focus on others like Coulomb interactions. In the first experiment, Fourier transform infrared spectroscopy will be used to compare bound model films with unbound ones. The spectra will be directly compared to identify possible changes, which could help to understand the bonding mechanisms taking place.

In context of the model system, bonds of xylan-cellulose and xylan-xylan surfaces are much stronger than their cellulose-cellulose counterparts, especially when swelled in ionic water. This was shown by Rohm et al. [23] using cellulose model films, xylan model films and different swelling water compositions. The

reason is not fully understood. The other two experiments in this work use a novel approach to adsorb xylan on cellulose model films. It will be tested if these xylan adsorbed films also show increased bonding strength compared to pure cellulose. First, quartz crystal microbalance with dissipation was used to analyse the adsorption process in detail. Then, tensile tests were conducted to determine the bonding strength between bound xylan adsorbed model films.

2 Method

2.1 Cellulose model films

One of the first tasks in this work was to get familiar with the fabrication of cellulose model films and possibly improve the process to create similar and homogeneous high quality films. This fabrication process, the swelling and drying routine, the xylan solution and the other resources used will be discussed in the following subsections.

2.1.1 Trimethylsilyl cellulose

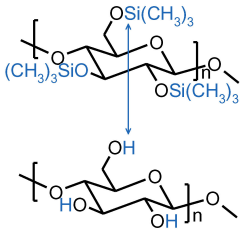

Figure 2.1: Comparison of TMSC and cellulose.

The method described by Kontturi et al. [17] relies on the chemical compound trimethylsilyl cellulose (TMSC). In TMSC, the hydrogen atoms of the free OH groups of cellulose are exchanged by trimethylsilyl groups which are three methyl groups bonded to a silicon atom (see figure 2.1). In contrast to cellulose, it is soluble in toluene and it can be used to create thin TMSC layers by spincoating a toluene-TMSC solution on a substrate. These TMSC layers can be converted to cellulose by regeneration using hydrogen chloride.

2.1.2 Raw materials and equipment

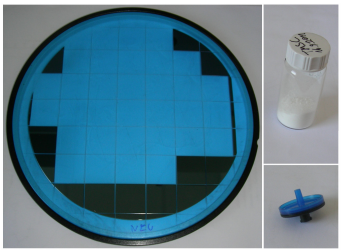

Figure 2.2: Equipment; silicon wafer pieces in plastic packaging, TMSC (white powder) and a 0.45 μm filter.

TMSC was bought from the German company "Thüringisches Institut für Textil- und Kunststoff-Forschung e.V." (TITK). They sell TMSC fabricated from micro-crystalline cellulose (MCC) with a degree of substitution of 2.9 ± 0.1. MCC is native cellulose with "partially degraded chains", which have a DP of 150 to 300 [13, p. 3361]. The MCC source plays an important role, because the TMSC concentration in toluene needed to create homogeneous high quality films varies with different sources. The MCC used by TITK to synthesise TMSC was the microcrystalline cellulose powder "Avicel" used in food or pharmaceutical industry. Ten grams of TMSC were bought in December 2011, another ten grams were bought in October 2013. Silicon wafers were used as a substrate and bought from the company Siegert Consulting. They were doped with boron and the surface had a <100> orientation. The wafer thickness was (675 ± 25) μm and they were cut in squared 2 cm^2 pieces. At last, toluene with a purity of 99.6%, HCl (37%) from Sigma Aldrich, the spincoater "CT62" from Karl Suss and "Chromafil Xtra" 0.45 μm filter were used in the fabrication process. Figure 2.2 shows the silicon wafers (in plastic packaging), the TMSC (white powder) and a filter.

2.1.3 Fabrication

The suggested process [17] was modified slightly. The actually applied procedure is listed below. Several test runs with different parameters were executed to compare the film quality. It turned out that the TMSC-toluene concentration and spin coating speeds are the most important factors. A 5 g/l (or lower) concentration combined with spin coating speeds of 3000 to 4000 rpm clearly showed the best results. Figure 2.3 shows examples of the test samples with

different concentrations. Changes in surface homogeneity are noticeable. The concentration 5 g/l was a compromise between film quality and thickness. With lower concentrations, higher film qualities are possible, but one would have to add more layers to achieve a certain thickness - which results in a longer fabrication process. For the planned infrared measurements, thicker layers were needed (at least 100 nm). Generally, the following procedure was used:

1. Fabrication of a 5 g/l TMSC-toluene solution (usually about 5 ml).
2. Mixing the solution over night using a magnetic stirrer.
3. Filtering the solution with 0.45 μm filters.
4. Cleaning of silicon wafer surface with acetone.
5. Spin coating of 50 to 170 μl solution (depending on sample size) for 60 s with 4000 rpm and 2500 rpm/s onto the silicon wafer.
6. Regeneration for ten minutes in a small Petri dish with 1 ml 10 % HCl.
7. If thicker layers are needed: Return to Step 5.

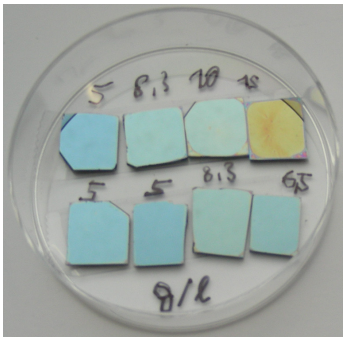

Figure 2.3: Cellulose model films fabricated with different TMSC-toluene concentrations (5.0, 6.5, 8.3, 10.0 and 15.0 g/l).

To verify stable conditions, solutions stored longer than three days were not used again. For every coating session, a new 10% HCl solution was prepared from the 37% HCl source. Furthermore, the regeneration was once verified via the contact angle of a water droplet.

2.1.4 Swelling and drying

The swelling of the cellulose model films was done in a beaker (8 cm diameter) with distilled water (fill height about 1 cm) covered with aluminum foil. The standard procedure for the first experiment was twelve hour swelling followed immediately by a four hour drying session. For drying, a “Rapid Köthen” sheet dryer from Paper Testing Industry Gmbh (model RK-4A) was used (shown

in figure 2.4). The samples were paired on top of each other (like a sandwich) and placed in the device between teflon and paper sheets (see right side of figure 2.4). The temperature in the device was set to 92 °C and a pressure of 0.1 bar was realised through a water jet pump. After this procedure, the two cellulose model films are bound and form one sample. This will be generally called "bound" sample. In case of tensile tests, the samples were stored at a climate chamber (40.5% relative humidity and 23.8°C) before testing for twenty four hours. This swelling & drying routine was adopted from chapter 2 in Rohm [22].

2.1.5 Xylan adsoprtion

Figure 2.4: The sheet drier, the right side shows a typical sample arrangement on teflon and paper sheets.

A main topic in this work is the influence of adsorbed xylan on cellulose model films. In the theses from Djak [6] and Rohm [22], xylan layers have been spincoated onto the cellulose model films using a dimetyl sulfoxide solution. Here, another approach is used. Xylan is adsorbed onto cellulose model films using a 0.5 g/l alkaline aqueous xylan solution with 1 mMol NaCl. The pH of the solution was adjusted to 8 by sodium hydroxide. The xylan was provided by the company "Lenzing AG" and was extracted from a beech sulfite dissolving pulp with an average molecular weight of 9.0 kDa. It had a xylose content of 90%, 4.8% uronic acid residues, 0.8% glucose and 0.4% mannose. To adsorb the xylan from the solution on the cellulose model films, the samples were rinsed with it in different ways (depending on the experiment). Two types of these solutions were created by filtering it using a "Chromafil Xtra" 0.45 μm filter to see possible differences in upcoming experiments. The concentration and NaCl content of the solution is crucial and influenced by the results in chapter 3.2.2 in the work of Djak [6].

2.2 Fourier transform infrared spectroscopy

Results of Fourier transform infrared spectroscopy (FTIS) on this type of cellulose model films are already present in literature. Schennach et al. [26] presented a new polarisation modulation technique which can be used to analyse such cellulose model films in a range of 400 to 4000 wavenumbers. One of the first applications of this method was the master's thesis of M. Djak [6], he examined several types of cellulose and xylan films and compared the findings to literature data. One intention in this work is to create a comparison of bound and unbound cellulose model film spectra using this method. Is there a significant change in the spectrum of a cellulose model film after creating a bond through water-swelling & drying? A short introduction into the physical principle of infrared spectroscopy will be given first. It will be mainly based on books by Demtröder [5, chapter 9.9 and 10.1.1] and Griffiths et al. [10, chapter 1.2 and 2.1 to 2.4]. The measurement routine and the equipment will be presented afterwards, the results will be discussed in chapter 3.1.

2.2.1 Vibrating molecules

"Electromagnetic radiation is emitted from any substance at non zero temperature." [1, p. 247]. At room temperature, a bigger part of this radiation is in the infrared region and is caused by molecular oscillations resulting from kinetic energy of the atoms - which they always have at a non zero temperature. Every atom in a molecule has 3 degrees of freedom, which means that the molecule itself has $3N$ degrees of freedom. Translation and rotation of the whole molecule takes six degrees of freedom. As a logical consequence, a non-linear molecule (bond angles unequal 180°) has $3N - 6$ degrees of freedom to oscillate. The resulting molecular modes of oscillation have specific energy states. A transition between those energy states may lead to emission of radiation in the IR range (or vice versa). The energy of fundamental vibrational energy states relates to radiation in the medium infrared region (400 to 4000 wavenumbers). Such an interaction is only possible, if the dipole moment of the molecule changes

during the vibration. This is a general requirement for IR activity and can be explained through conversion of momentum via quantum mechanics which is beyond the scope of this introduction. [5, pp. 248–249, 10, p. 3]

Specific details of molecular oscillations can be seen in infrared spectra, they are typical for certain molecules or chemical functional groups. This can be used to analyse IR active materials and identify or compare their molecular composition - one of the main applications of IR spectroscopy. Instead of the physical quantity frequency and its unit Hertz - a commonly used alternative in IR spectroscopy - is the inverse wavelength and its unit wavenumber. A wavenumber gives "the number of waves per unit length", the unit length is usually centimetre. [10, pp. 4–5]

2.2.2 The FTIR method

Fourier spectroscopy is two beam spectroscopy based on a Michelson interferometer [5, p. 364]. Figure 2.5 shows the layout of such an interferometer. An incoming light beam is separated in two beams using a beam splitter. Then, both beams are reflected back to the splitter by mirrors at a certain distance. Ideally, the reflection by the mirrors leads to a 180° phase shift of the light (at normal incidence), while the reflection by the beam splitter leads to a 90° phase shift (transmission through the beam splitter causes no shift). If the distance of the mirrors to the beam splitter is the same, the full intensity of monochromatic light would go to the detector, because the total phase difference between the two beams result in constructive interference at the detector and destructive interference at the source. [10, p. 22]

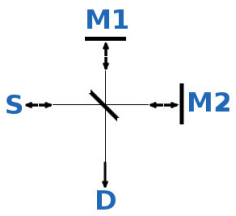

Figure 2.5: Draft of a Michelson interferometer, showing fixed mirror (M1), moveable mirror (M2), detector (D), source (S) and beam splitter (middle).

When moving one mirror at a constant speed in the same direction, the signal at the detector will show an intensity change depending on the distance of the

mirror to its original position. This is because only one of the interfering beams has to travel a longer path which changes their phase difference at the detector. The displacement of the mirror is called retardation. If the speed of the mirror "is greater than 0.1 $cm \cdot s^{-1}$", the device is called a "rapid scan interferometer" [10, p. 20]. The output signal at the detector is called interferogram and contains full information of the spectrum. The spectrum can be calculated out of the interferogram using a mathematical tool called "Fourier transformation" which explains the name of the method. [5, p. 365]

This approach is not restricted to monochromatic light, in fact, continuous light sources are used in infrared spectroscopy. For an exact quantitative solution in this case, the movable mirror would have to travel an infinite way which is not possible. To overcome this problem, the output signal is multiplied with a function of retardation, which is zero outside the maximal/minimal mirror position and non zero in between. This causes side effects in form of distortions in the spectrum, but they can be minimised by finding optimal shapes for this so called "apodization function". All these calculations are usually processed by a computer in real time during the measurement. However, the final spectral resolution of the device is still limited on the maximum retardation and other factors, for example misaligned mirrors or inaccuracies connected to the movable mirror. [5, p. 366–367]

2.2.3 Equipment

The spectrometer used was a Bruker IFS 66v/S (rapid scan interferometer) with a modular transmission and reflection unit. These units are shown in figure 2.8, the beam path is indicated by blue lines. The angle at which the light hits the sample can be modified by adjusting the mirrors. The units can be mounted into the sample chamber of the spectrometer as a whole - the mounted reflection unit is shown in figure 2.6. The manual of this spectrometer states a resolution better than 0.25 cm^{-1} if apodized. The beam path contained two polarisation filters - the standard polariser of the spectrometer - a thallium

bromo-iodide (KRS-5) mesh and an additional gold wire grid polariser. The gold wire polariser was set manually to a fixed position and the other one was controlled electronically by the spectrometer software to generate s- and p-polarised signals. Both filters are shown in figure 2.7. The sample chamber and the optical setup were evacuated to (0.04 ± 0.1) mbar by a rotary vane pump. The infrared light was created by a silicon carbide glowbar (SiC) and detected by a mercury cadmium telluride detector cooled by liquid nitrogen (label B in figure 2.6 shows the nitrogen inlet). The operating range of such a detector lies roughly between 500 and 4000 wavenumbers (if sufficiently cooled). For more details about this setup, refer to chapter 2.1 in the master's thesis of E. Gilli [9].

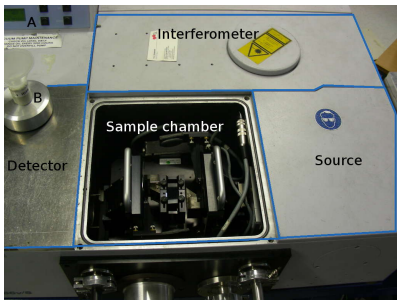

Figure 2.6: Top view of a "Bruker IFS 66v/S" with a mounted modular reflection unit; A . . . vacuum control, B . . . inlet for liquid nitrogen.

2.2.4 Measuring routine and parameters

First of all, the mirror positions of the reflection unit were optimized for maximum intensity (using a silver mirror sample in reflection). Following, the polarisers were set up using a spectrometer software macro that switches the angle of one polariser by a certain amount of degrees between 0 and 180° while doing measurements in between each step. This generates spectra with different intensities, which can be used to calibrate the polariser positions. For more details about this procedure refer to chapter 2.1.4 in the thesis of M. Djak [6]. For all measurements an incidence angle of 74° and an

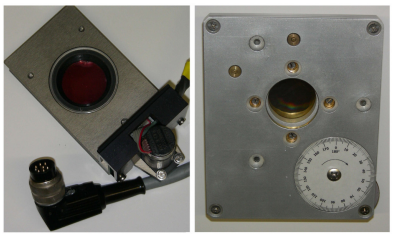

Figure 2.7: KRS-5 mesh polariser (left) and gold wire grid polariser (right).

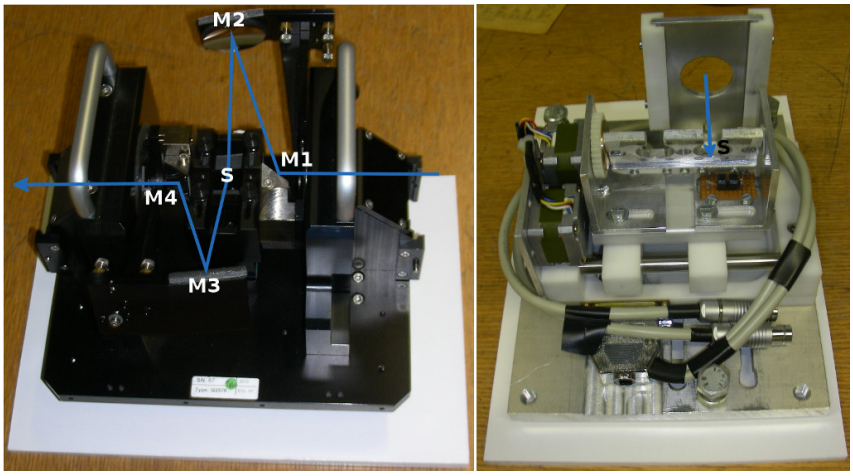

Figure 2.8: Modular reflection (left) and transmission unit (right) used in the experiments, the beam path is indicated; M . . . Mirror, S . . . Sample.

aperture size of 4 mm were used. The decision to use this incidence angle is based on the discussion in chapter 3.1.1 in Djak [6].

The following list summarises a typical measuring process:

1. Starting to cool the detector using liquid nitrogen.
2. Venting the sample chamber (it is usually evacuated while idle).
3. Mounting the transmission/reflection unit including sample.
4. Checking mirror positions (incidence angle) and polarisation filter angle.
5. Evacuating the sample chamber.
6. Starting the measurement using the spectrometer software.

Generally, background signals were measured using a blank silicon wafer piece. In case of bound samples, this was done by using two blank silicon wafer pieces on top of each other. The wafers were cleaned with acetone before measurements. The backgrounds were measured directly after the corresponding samples to minimise changes in temperature, humidity and other environmental side effects. It was made sure that the silicon wafer piece used for the background was similar to the one in the sample (e. g. both single side polished).

As a first attempt to check the signal strength, see which cellulose thickness was

needed and to practice the routine, several test samples with different cellulose thicknesses (different number of stacked layers) were created and measured. As a further step, the measuring process including bound samples (as described in chapter 2.1.4) was tested. Several samples have been created and measured before and after a swelling & drying step. It turned out that a critical part in this measurement was the mounting of the dried sample into the spectrometer sample chamber - because the sample could be easily broken during this process. After these test runs, several measurements were conducted, in total four series using two to four samples each were done. One measurement generates two output files, the p- and s-polarised spectra. These output files are actually five averaged measurements each (done automatically by the software). Every output file contains two rows of data (inverse wavelength and intensity) which were exported and analysed using the software “Matlab”.

2.3 Quartz crystal microbalance with dissipation

First attempts to characterise xylan adsorption on cellulose model films through "Quartz crystal microbalance with dissipation" (QCM-D) measurements were made by M. Djak [6]. Low xylan concentrations of 10 and 100 mg per litre were used (unsaturated solutions) which showed no xylan adsorption onto the cellulose surface. Adding salt (NaCl) into the solution showed better adsorption behaviour. A possible explanation of this is shielding of negatively charged molecular groups of cellulose through the Na^+ ions [6, p. 78]. In this work, QCM-D measurements were conducted using an adapted xylan solution based on the results of M. Djaks work.

2.3.1 The QCM-D principle

"The thermodynamically stable form of silicondioxide (SiO_2) at temperatures up to 573 °C" forms a trigonal crystal which is named α-quartz [2, p. 117]. This material has a history as an acoustic resonator for more than one hundred years [2, p. 125]. Because of the trigonal structure being a low form of symmetry (lack of a centre of symmetry), quartz is an anisotropic material, furthermore it is piezoelectric. It has different temperature coefficients of thermal expansion in different crystal directions. This can be used to realise standing acoustic waves with low temperature dependence by cutting the crystal in a certain shape. These standing waves can be coupled piezoelectrically and can have very low energy losses [2, p. 126]. Of course, there are several modes possible in a disc like structure - some are more suited for resonator purpose - like the thickness shear mode. Figure 2.9 shows the assignment of the axes in a quartz

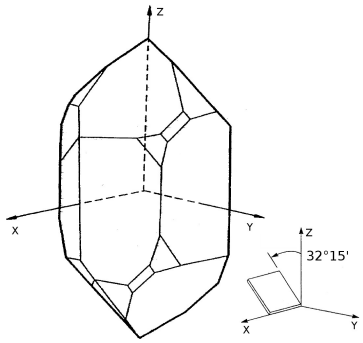

Figure 2.9: The assignment of axes to a quartz crystal and the AT-cut angle [19, p. 663-664].

crystal and a specific cutting angle for the so called AT-cut (T stands for temperature). If a disc is cut out of a crystal using this angle in respect to the crystal axes, very temperature stable thickness shear waves can be excited by including the crystal into an oscillation circuit with a frequency near to its eigenfrequency. These waves propagate perpendicular to the crystal surface. [19, p. 663–664]

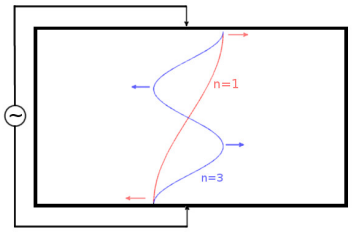

Figure 2.10: Electrically excited quartz crystal, showing an indirect transversal piezo effect

Figure 2.10 outlines this scenario - indicating the fundamental acoustic oscillation (red) and its third overtone (blue) of a quartz slab, driven by an electric circuit. Here, the crystal gets excited electrically in the polar axis (x-axis) and shows a mechanical response in the y-axis - the so called mechanical axis [3, p. 205]. Because of its stability, this is the intended mode in QCM devices. Depending on the thickness, several fundamental frequencies can be obtained. For AT-cut crystals, this range reaches from 1 to 250 MHz [3, p. 220]. Because the thickness of the quartz slab is limited by economical aspects to about 0.08 mm, higher frequencies than 20 MHz are usually realised through overtones of the fundamental oscillation. One can excite only odd overtones electrically, for even ones the poles at the surfaces would be the same. [3, p. 221]

Figure 2.11 shows a draft of a typical modern quartz resonator, like it was used in this work (14 mm diameter and 0.3 mm thickness). It has gold electrodes attached to it on both surfaces. Of course, such electrodes influence the system (its eigenfrequencies) and it has to be balanced out somehow, but these aspects are beyond the scope of this introduction. The eigenfrequency of the thickness shear mode is 5 MHz - a commonly used resonance frequency in modern devices.

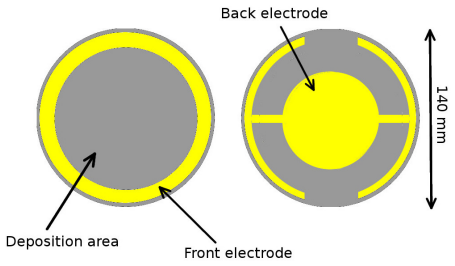

Figure 2.11: A draft of a modern QCM-D sensor - showing front and backside [21].

If mass is added to such a device, this has a direct relation to the reso-

nance frequency under certain circumstances, as shown by G. Sauerbrey in 1959 [24]. "Provided that the mass is (i) small compared to the weight of the crystal, (ii) rigidly adsorbed, and (iii) evenly distributed over the active area of the crystal" [28, p. 426], the Sauerbrey equation 2.1 describes a direct proportional relation between mass (Δm) and frequency change (Δf).

$$\Delta m = \frac{C}{n}\Delta f \tag{2.1}$$

The constant C is calculated from the quartz density, thickness and eigenfrequency (C ≈ 17.7 ng Hz^{-1} cm^{-2} for 5 MHz crystals [28, p. 426]). This equation is also valid for overtones (n ∈ ℕ) of the fundamental oscillation. For gas phase and vacuum applications, the conditions of the Sauerbrey equation might be satisfied. In case of mass adsorption from the liquid phase, this is not the case. As a result, a new technique has evolved, which includes the measurement of the energy dissipation in the crystal parallel to the frequency change. [28, p. 427] The quality factor of such a plain quartz crystal is high (a design goal) which means that the crystal oscillation has a low dampening (less energy dissipated). When a non rigid layer is attached to the crystal, its oscillation is dampened heavily. One can use the width of the resonance peak to determine dissipation. [28, p. 427–428] But the preferred option is to measure the dampening of a freely oscillation quartz crystal by periodically switching the driving force on and off (figure 2.12). Figure 2.13 gives an overview of the measurement setup as described by Hook et al. [11, p. 966]. Basically, the electronics let the quartz decay near its resonance mode. The output signal (A in equation 2.2) is superimposed by a reference frequency and fitted by a exponentially dampened sinusoidal by a computer. The dissipation can be calculated from the output signal and is defined in

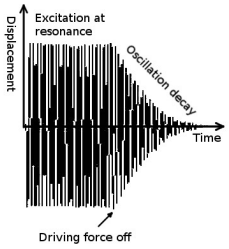

Figure 2.12: Schematic of the acoustic oscillation in a quartz crystal before/after switching off the driving force [28, p. 429].

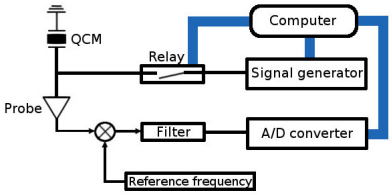

Figure 2.13: Schematic illustration of the setup in a QCM-D experiment [11, p. 966].

equation 2.3. Q is the Quality factor, E_{store} is the energy stored in the oscillating system, E_{diss} is the energy dissipated during one period of oscillation (τ), f is the frequency, t is the time and β is the damping ratio. [11, p. 967]

$$A(t) = A_0 e^{\beta t} sin(2\pi f t + \alpha) \tag{2.2}$$

$$D = \frac{1}{Q} = \frac{\beta}{\pi f} = \frac{1}{\pi \tau f} = \frac{E_{diss}}{2\pi E_{store}} \tag{2.3}$$

2.3.2 Equipment and setup

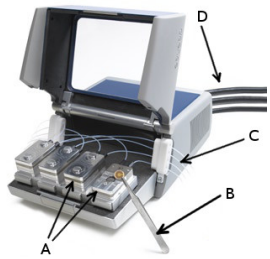

Figure 2.14: QCM-D device "E4" from Q-Sense [20].

The QCM-D experiments done in this work use the same approach as described in the last chapter 2.3.1. A modern setup from the company "Q-Sense" was used to measure dissipation and frequency change of a cellulose coated quartz crystal during xylan adsorption from the liquid phase. The cellulose model films were - in principle - fabricated as described in chapter 2.1.3. Single cellulose layers were spincoated onto quartz crystals. A 0.5 g/l alkaline aqueous xylan solution (see chapter 2.1.5) was prepared for the adsorption step. Using a "Q-Sense E4." quartz crystal micro-balance with dissipation monitoring and a flow module - four samples were examined at the same time. Figure 2.14 shows this device. Label A indicates two opened/closed flow modules, B a sample holder, C the tubes coming from the pump and D the wires to the electronic unit. Figure 2.15 shows two opened/closed flow modules in more detail, label B points at a mounted quartz crystal. For all measurements, 5 MHz quartz crystals with gold electrodes - fabricated by Q-Sense - were used. The sample chamber was temperature-monitored and the flow module was driven by a peristaltic pump (from "Ismatec") generating a flow rate of 0.1 ml/min. Furthermore, a "Millipore-Direct 8" device was used to fabricate purified water with a resistivity greater than 10 MΩcm at 25

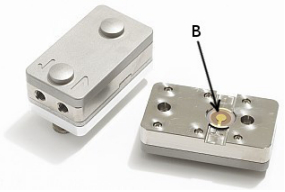

Figure 2.15: Two flow modules (closed & opened) [21].

℃ (used for water rinsing steps). The measurements were all done in a row and took about four hours, with a room temperature (measured inside the sample chamber) of 21 ℃. The software of this device was named “Q-Soft 401”. Another software called “Q-Tools” - mainly used for advanced data analysis and modeling - was not used in this work. Instead, the data were analysed in Matlab.

2.3.3 Execution

The experiment started with a functionality check of the quartz crystals, these crystals are very sensitive to environmental influences and often show malfunctions (e. g. an unstable eigenfrequency). After passing this test, the cellulose layers were added to the samples and they were mounted again into the device. Now, several constitutive rinsing/adsorption steps using purified water, heavy water, aqueous alkaline solution, and aqueous alkaline xylan solution were made while the frequency and dissipation change was monitored (maximum time resolution of 200 data points per second). The course of events will be described in more detail in chapter 3.2 introducing the results of the measurements.

2.4 Tensile tests

One simple approach to examine surface interactions of cellulose is to measure the tensile force needed to separate two bound model films. This idea was realised by S. Rohm in his master's thesis [22], using a powder rheometer. In particular, xylan and cellulose model films were fabricated (both using spincoating) and bound together through swelling & drying using different ionic compounds in the swelling water. Then, the tensile strength needed to separate those samples was measured and analysed. The difference in this work is that xylan was adsorbed (instead of spincoated) on existing cellulose model films using an aqueous xylan solution containing salt. The goal was to create xylan adsorbed model films for tensile testing similar to the QCM-D experiments.

Figure 2.16: Xylan adsorption using a magnetic stirrer.

2.4.1 Preparations

To do such an experiment, several one-layered cellulose model film samples were prepared. The usual procedure was used (see chapter 2.1.3), only the sample size was reduced to squared (1.0 ± 0.1) cm wafer pieces for practical reasons. Before testing, a beaker was cleaned using acetone, rinsed and filled with purified water. The model films were swelled in it for one hour (or 30 minutes). After that, the water was replaced with a xylan solution (usual type, see chapter 2.1.5) for 30 minutes. For better adsorption conditions, a magnetic stirrer was used during this step. Figure 2.16 shows this arrangement during xylan adsorption. An optional 30 minute (purified) water rinsing step followed (same as water

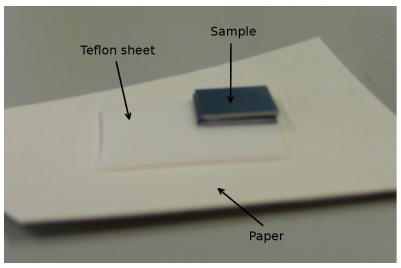

Figure 2.17: Sample on teflon and paper sheet before drying.

swelling, but with a magnetic stirrer). Now, the samples were put out one by one and arranged on teflon sheets on top of each other (see figure 2.17). Directly after that, the teflon sheets (with the stacked samples) were put into the Rapid Köthen dryer for four hours (see chapter 2.1.4). Finally, the samples were stored in a climate chamber (40.5% relative humidity and 23.8°C) for one to three days before starting the tensile tests. The samples were transported in air-proof plastic boxes to minimise environmental influence like higher relative humidity.

2.4.2 Test execution

The same procedures and the same equipment as developed by S. Rohm were used. In depth information on the method and its development can be found in the works of S. Rohm [22, 23]. To start the experiment, the piston of a Freeman technology FT4 powder rheometer was prepared with double sided tape. The samples were mounted onto the rheometer socket using the same type of double sided tape. Figure 2.18 is displaying this situation. The piston is built up of multiple parts, namely three springs, two spacers (plastic cylinders) and a plastic winding. These parts are shown in figure 2.19a, especially the springs play an important role, because they modify the force - length dependence. This will be discussed in more detail using the results in chapter 3.3. To start a tensile test, a software macro was activated, which moved the rheometer bar down at constant speed (0.02 mm/s) until contact was made. Figure 2.19b is showing a closer position before contact. After contact, the force was increased up to a maximum of (40 ± 10) N, held for about 20 seconds and reduced back to zero. At zero force, the actual tensile test started and the rheometer

Figure 2.18: Powder rheometer with mounted sample.

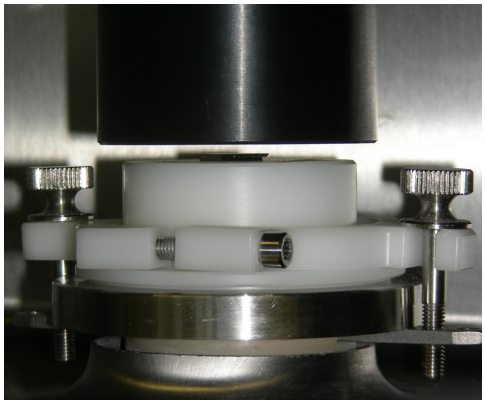

(a) Rheometer piston, socket and sample a few millimetres before contact.

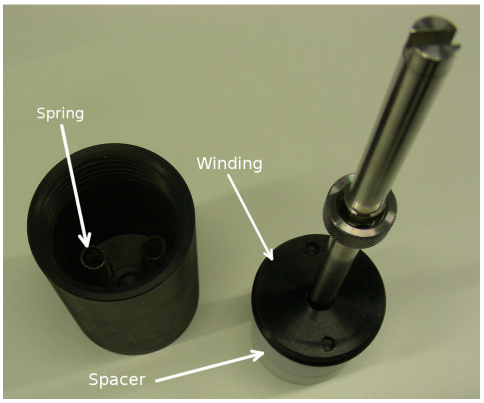

(b) Parts of the rheometer piston: Springs, spacers and winding.

Figure 2.19: Rheometer socket, piston and bar in detail.

bar was moved upwards (negative force by definition). After the separation of the sample, the process was usually stopped manually to save time. Such a test took about ten minutes per sample. The Force and the length variation applied to the rheometer bar were measured five times a second and saved in a data file. For calibration, a measurement with two blank samples bound together using cyanacrylate glue was made. This can be useful for binding energy determinations, because some energy is absorbed by the double sided tape. Besides that, it can act as a test run to check the rheometer functionality before using actual samples.

3 Results and discussion

3.1 Comparison of bound and unbound cellulose model films using polarisation modulated Fourier transform infrared spectroscopy

In this section, the results of the FTIR measurements introduced in chapter 2.2 will be covered. Table 3.1 lists the measurements done in chronological order. An additional horizontal line in the table means a break of at least one day in the process. New background measurements were made after such breaks. Generally, for every series a background of each measurement mode (transmission/reflection) and sample type (bound or unbound) was made. The backgrounds are not noted in table 3.1. After a short overview of the data set, the results will be discussed in more detail.

The first series consists of a six layer, a ten layer and two eight layer films which were measured in reflection and transmission. The two eight layer films were bound together but broke during the mounting process into the sample chamber of the spectrometer. Nevertheless, the transmission spectra of this broken sample was recorded. For the second series two new eight layer samples were created and measured in reflection/transmission. They were bound and measured again. Additionally, the six and ten layer samples of series 1 were bound and measured in this process. This series was not considered optimal, because there were handling mistakes with the 8-layer samples - which resulted in fingerprints and dust on the surfaces. Furthermore, streaks appeared in the swelling water (this could be a consequence of surface contamination).

Table 3.1: Chronology of spectroscopy experiments - divided into four measurement series. Different samples in a series are named a, b, c or d. If swelled & dried, two letters of the underlying samples are written together (e. g. "ab"). T stands for transmission and R for a measurement in reflection.

Experiment	Sample number	Sample type	Mode
Series 1	1a	6 layer	R
	1b, 1c	8 layer	R
	1d	10 layer	R
	1b, 1c	8 layer	T
	1bc	bound (broken)	T
Series 2	2a, 2b	8 layer	R
	2a, 2b	8 layer	T
	2ab	bound	T
	2ab	bound	R
	1ad	bound	T
	1ad	bound	R
Series 3	3a, 3b, 3c, 3d	8 layer	T
	3a, 3b, 3c, 3d	8 layer	R
	3ab, 3cd	bound	T
	3ab, 3cd	bound	R
Series 4	4a, 4b	10 layer	T
	4c	1 layer	T
	4a, 4b	10 layer	R
	4c	1 layer	R
	4ab	bound	T

Because of these circumstances, another attempt (series 3) was prepared. Four eight layer samples were fabricated, measured in reflection and transmission, bound and measured again in both modes. This time - no samples broke and surface contamination was minimised. After a review of the series 3 data, another possible contamination was identified. The samples were mounted on the spincoater using double sided tape. As a result the backsides of the samples were contaminated by glue (from the tape). Series 4 was done to eliminate any of this influence. Using another spincoater (with a working vacuum mounting mechanism) two ten layer samples were fabricated. Furthermore, newly purchased TMSC (same type) and double side polished silicon wafers were used this time.

After this overview of the experiments, the results will be outlined. To start with, the raw data of all measurements were plotted and quickly reviewed. In transmission, one could assume that the backgrounds should have the highest intensities - followed by the plain samples. The bound ones should have the lowest intensity. For example, figure 3.1 shows this with the p-polarised raw data of series 3 in transmission. Here, the backgrounds are indicated black, the plain samples red and the bound samples purple. Figure 3.2 shows the s-polarised reflection raw data of series 3. Due to reflection, the intensities differ and one can clearly see interference patterns caused by a Fabry Pérot effect of the sample structure. As a next step, all spectra have been divided by their backgrounds and their intensity maxima. Generally, the transmission spectra seemed to have less interference patterns, less noise and more noticeable absorption bands. As a result, the transmission spectra will be focused on in this analysis. At a later point, the reflection spectra will be briefly taken into account - based on the transmission results.

A main task is the classification of cellulose peaks. Similar experiments have been done already (also with the same type of model films) and numerous literature data is available for comparison. First, one needs to eliminate silicon oxide and air absorption bands. This has already been achieved by the division of the data by the backgrounds. At the beginning, peaks caused by contamination's (e. g. glue) were marked. For this, a silicon wafer with double sided tape has

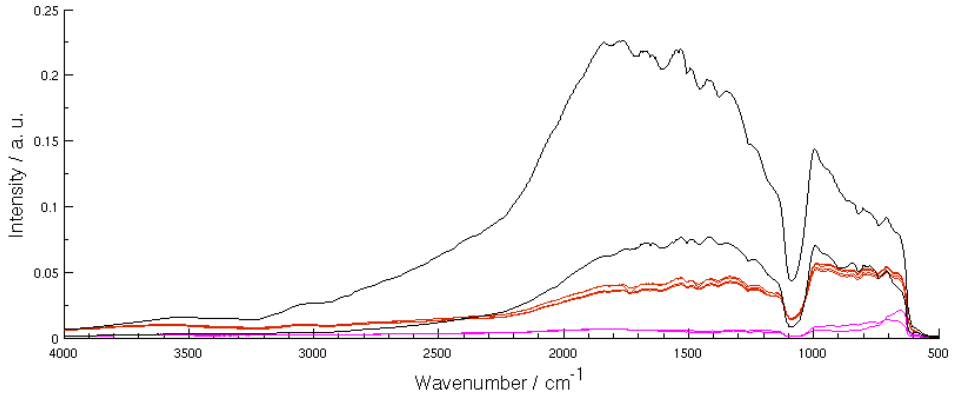

Figure 3.1: Raw p-transmission spectra of series 3

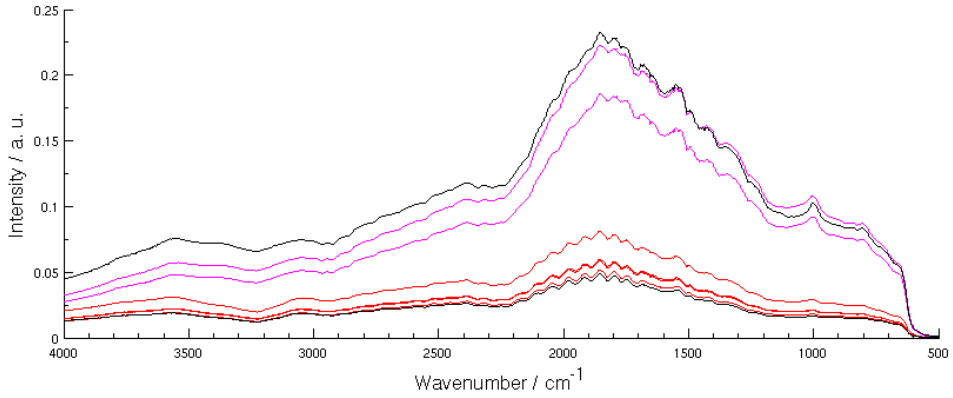

Figure 3.2: Raw s-reflection spectra of series 3

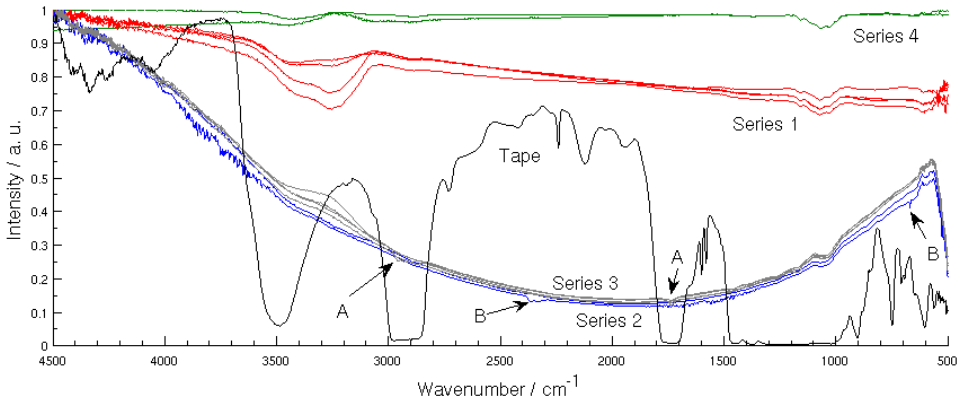

Figure 3.3: P-polarised transmission spectra of samples before swelling & drying compared to a spectrum of double sided tape.

been measured in transmission (this additional experiment is not listed in table 3.1). Figure 3.3 shows the whole p-polarised transmission spectra of all series before swelling & drying including the spectrum of the double sided tape (series 1 in red, 2 in blue, 3 in grey, 4 in green and the tape spectrum in black). This clearly indicates that the range of 1670 to 1700 wavenumbers and 2800 to 3000 wavenumbers is affected by glue contamination (these bands of series 3 are marked with an A in figure 3.3). Moreover, one spectrum in series 3 shows stronger peaks in those areas, which can be explained by a higher glue contamination of that particular sample. Series 4 (no glue contamination) does not show any noticeable absorption bands in these regions. Also the fingerprint/dust contaminated sample of series 2 sticks out (uncommon bands marked with B in figure 3.3). In the region of 3000 wavenumbers and higher, the spectrum shows more noise and absorption bands are hard to identify - they will not be discussed. Neither will be the range between 500 and 700 wavenumbers (high number of bands and end of the detector range reached depending on cooling). The remaining noticeable absorption bands after these exclusions are located between 850 and 1400 wavenumbers. Figure 3.4 shows the p-polarised spectra in this region (series 1 in red, 2 in blue, 3 in grey and 4 in green). In this representation, the spectra have been shifted in intensity for better comparability. The dashed green line in this figure is an additional

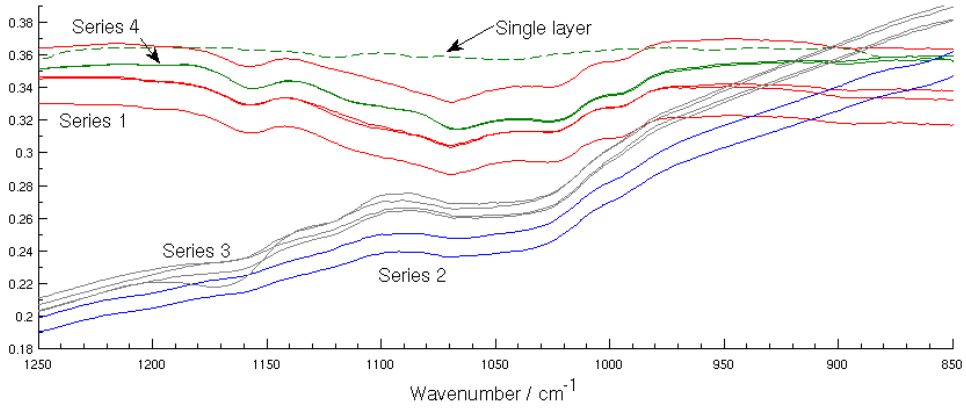

Figure 3.4: Transmission spectra of samples before swelling & drying; showing main cellulose adsorption bands while comparing all series in p-polarisation

measurement of a single layer cellulose model film (sample 4c in table 3.1). This sample clearly shows less absorption, which strengthens the assumption that these bands occur due to absorption in cellulose. Series 4 was used to assign the cellulose absorption bands occurring between 850 and 1400 wavenumbers by comparison with literature. Figure 3.5 shows the spectra of the two samples with clearly noticeable adsorption bands indicated in s- (green) and p-polarisation (dark green). Table 3.2 lists the band minima and their assignments.

The next step is the comparison with bound samples. Figure 3.6 shows this in the range of 850 to 1400 wavenumbers for series 4. The bound samples are drawn in purple (p-polarised dark purple, s-polarised light purple). The same peaks (which were identified before) are indicated in the figure. The bound sample spectra show a considerable sinus shaped interference pattern with a wavelength of about 1100 wavenumbers (figure 3.7 shows a broader range with about three wavelength of this oscillation). A corresponding Fabry-Perot etalon (two interfering layers in the sample) would have a length of about 4 to 5 microns (refer to chapter 3.1 in Gilli [9] for further details). It is believed that this is caused by the double side polished silicon wafers used in series 4. Because the relevant bands are still comparable, a background correction was omitted. Figure 3.8 shows series 3 (single side polished wafers) which does not show

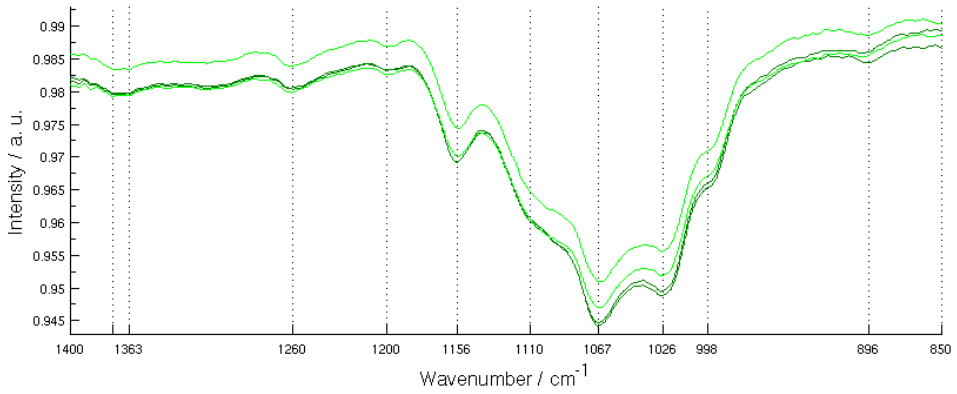

Figure 3.5: Transmission spectra of samples before swelling & drying; showing identifiable cellulose adsorption bands of series 4 in s & p-polarisation (green & dark green)

Table 3.2: Band minima (BM) of series 4 between 850 and 1400 wavenumbers, their assignments and literature reference.

BM/cm^{-1}	Band assignment	Literature reference
896	Antisymmetric out-of-phase ring stretching	899 cm^{-1} [14]
998	C-O, C-C stretching	1000 cm^{-1} [12]
1026	C-O stretching	1024 cm^{-1} [7]
1067	C-O stretching, O-H bending	1064 cm^{-1} [7]
1110	Antisymmetric in phase ring stretching	1110 cm^{-1} [12]
1156	Antisymmetric bridge C-O-C stretching	1159 cm^{-1} [14]
1200	O-H in plane bending	1200 cm^{-1} [7]
1260	CH_2 rocking	1254 cm^{-1} [6]
1363	C-H bending	1369 cm^{-1} [7]
1373	C-H deformation	1369 cm^{-1} [7]

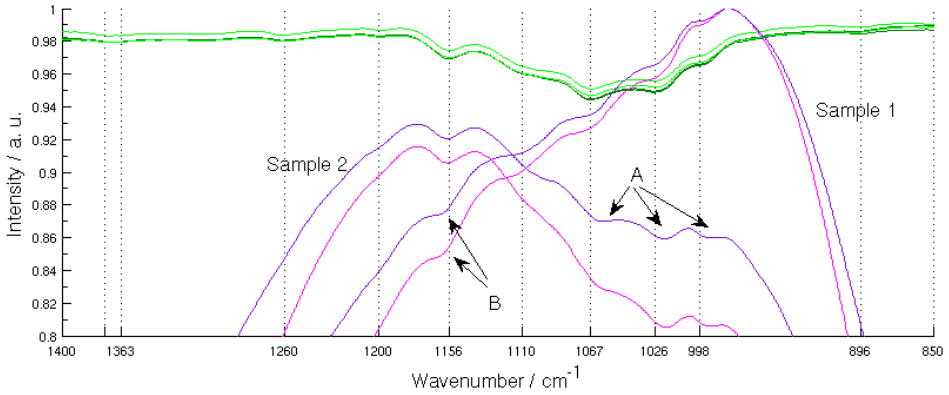

Figure 3.6: Comparison of model films of series 4 before (coloured in green) and after swelling & drying (purple). Showing main cellulose adsorption bands in transmission. S-polarised spectra are drawn in light green and light purple, p-pol. spectra in darker green and darker purple.

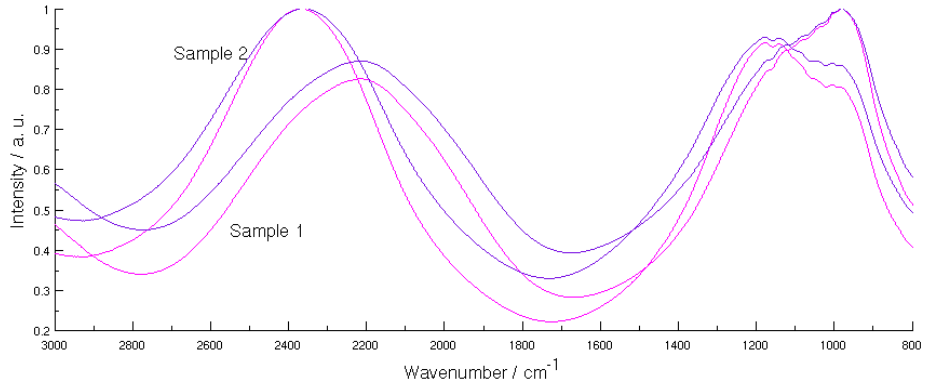

Figure 3.7: A better visualisation of the interference pattern overlaying the actual spectrum of the bound samples from figure 3.6.

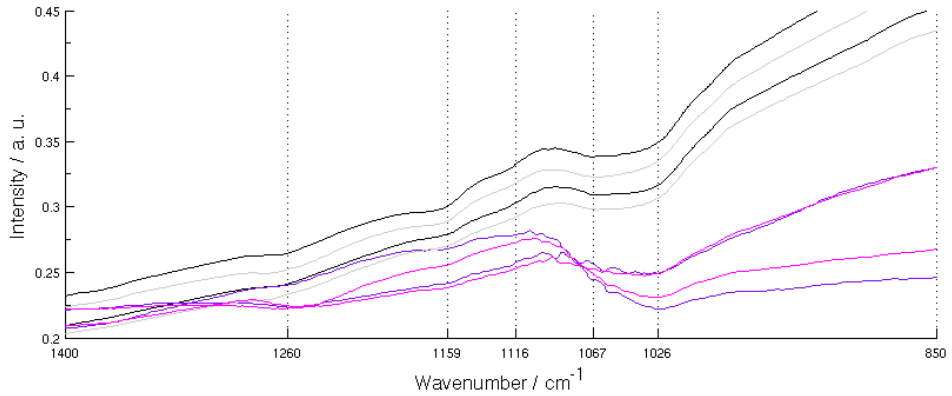

Figure 3.8: Comparison of model films of series 3 before (coloured in grey/black) and after swelling & drying (purple). Showing main cellulose adsorption bands in transmission. S-polarised spectra are drawn in grey and light purple, p-pol. spectra in black and darker purple.

such a large interference pattern. Besides that, series 4 shows better results and nearly all identified absorption bands are noticeable in the spectra of the bound samples, too. Some bands are shifted by a few wavenumbers (examples marked with A and B in figure 3.6). This could also be connected to the large intensity change superimposed by the interference pattern. Series 3 (figure 3.8) does not show all bands and the ones indicated are hardly observable. The same applies for the bound samples of series 2 and 1 which are not shown here.

As a last point, the reflection spectra will be discussed. The results of the transmission spectra showed worse quality for bound samples (more noise and interference effects). This makes sense, considering the imprecise background of two stacked silicon wafers including an air gap. If a measurement shows a different interference pattern in contrast to the background measurement (e. g. because of a large air gap between the samples), the background division would introduce a certain shape to the baseline of the spectrum. Compared to transmission, the outcome of the reflection technique is more dependent on polarisation, the incidence angle and surface properties of the sample. As a result, the reflection spectra generally show higher noise and more interference effects. Figure 3.9 shows the normalised reflection spectra of sample 4a and 4b

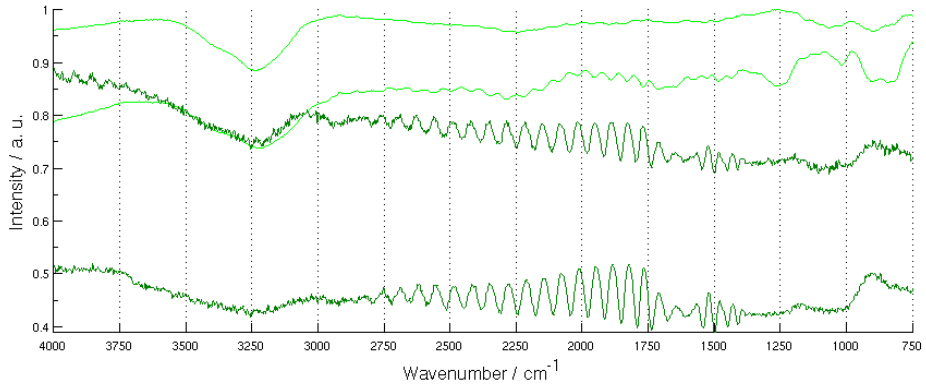

Figure 3.9: Reflection spectra of sample 4a and 4b in s- (light green) and p-polarisation (dark green).

in s- and p-polarisation divided by the background. Especially in the p-polarised spectra (dark green), interference patterns appear and the spectrum is noisy. This was observable in all reflection measurements. As a consequence, it is harder to distinguish between interference, noise and bands, which made the analysis of the reflection spectra difficult and explains the focus on the transmission spectra mentioned earlier. Figure 3.10 shows the s-polarised spectra of the samples 1a, 1b, 4a, 4b and 1ab in the range of 850 to 1400 wavenumbers. In the spectrum of the bound sample 1ab (pink), it is difficult to distinguish between interference pattern and bands. The minima at 900 and 1260 wavenumbers fit the bands determined in transmission (table 3.2). The minimum between 1050 and 1100 wavenumbers overlaps the transmission bands at 1067 and 1110 (table 3.2), but the shape is likely to be caused by interference. The unbound samples 1a and 1b hardly show noticeable bands, samples 4a and 4b show weak bands at 900 and 1260 wavenumbers. Figure 3.11 shows the p-polarised spectra of the same samples. The bound sample show similar bands as in the s-polarised spectrum. The unbound samples are also noisy and difficult to identify. Based on all these problems and the results of the transmission measurements, it was decided not to analyse the reflection spectra any further and focus on the other planed experiments.

To summarise this first experiment, the transmission spectra of bound and

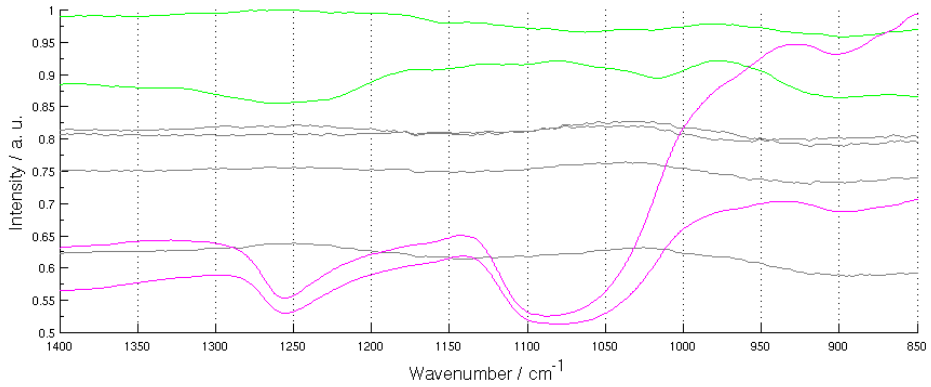

Figure 3.10: Comparison of bound/unbound reflection spectra in s-polarisation. Shown are samples 1a and 1b in grey, 4a and 4b in light green and the bound sample 1ab in light purple.

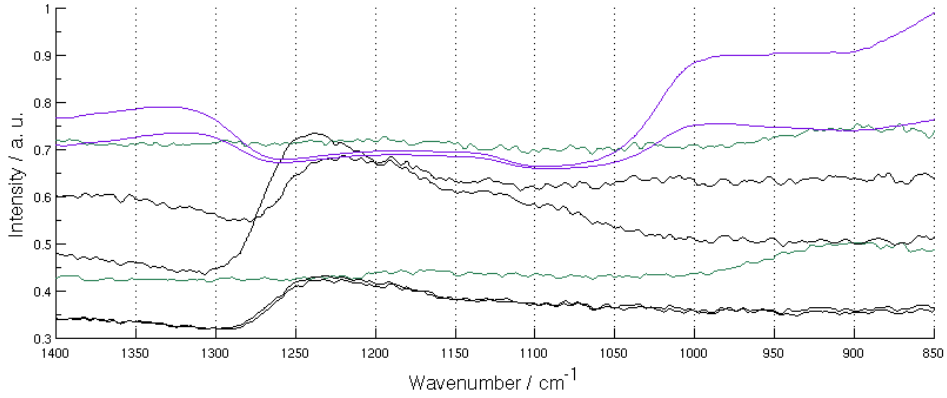

Figure 3.11: Comparison of bound/unbound reflection spectra in p-polarisation. Shown are samples 1a and 1b in black, 4a and 4b in dark green and the bound sample 1ab in dark purple.

unbound samples were successfully analysed and did not show significant differences in the range of important cellulose absorption bands between 850 to 1400 wavenumbers. Generally, the spectra of bound samples experienced more noise and interference effects - most likely caused by the stronger layered structure. This made a direct comparison difficult. The reflection spectra are affected by these aspects more severely, they showed generally worse results and did not lead to a viable comparison.

3.2 Analysis of xylan adsorption onto cellulose model films using quartz crystal microbalance with dissipation

The findings of the QCM-D experiment introduced in chapter 2.3 will be presented and discussed in this section, starting with a list summarising the course of events:

1. Functionality check of quartz crystals: First of all, four functional quartz crystals had to be found. For this, plain crystals were mounted into the sample chamber and the frequency was observed for a few minutes to determine functionality of each quartz crystal.
2. Adding the cellulose layers: As a next step, a single cellulose layer was added to each of the four quartz crystals. The same parameters and procedures described in chapter 2.1.3 were used. Then, the electrodes were cleaned with acetone and the frequency shift of the four coated samples was measured for about ten minutes.
3. Swelling of cellulose layers: Now, the flow module was activated and purified water was pumped through the system while measuring frequency and dissipation shift of the samples for about 30 minutes.
4. Heavy water exchange: The purified water was exchanged with heavy water and the experiment was continued for 30 minutes. As a preparation for the xylan adsorption, the heavy water was exchanged with purified water again (and rinsed for about 30 minutes).
5. Xylan adsorption: The samples were equilibrated in the basic aqueous alkaline solution. Then, two samples were adsorbed with a filtered xylan solution, the remaining two with an unfiltered one (see chapter 2.1.5 for details about filtering). After 30 minutes of xylan adsorption, the samples were rinsed again with the basic aqueous alkaline solution. A final rinsing step with purified water followed.

The functionality check of the quartz crystals was done for about ten minutes and figure 3.12 shows the results of all four samples using the 7^{th} overtone.

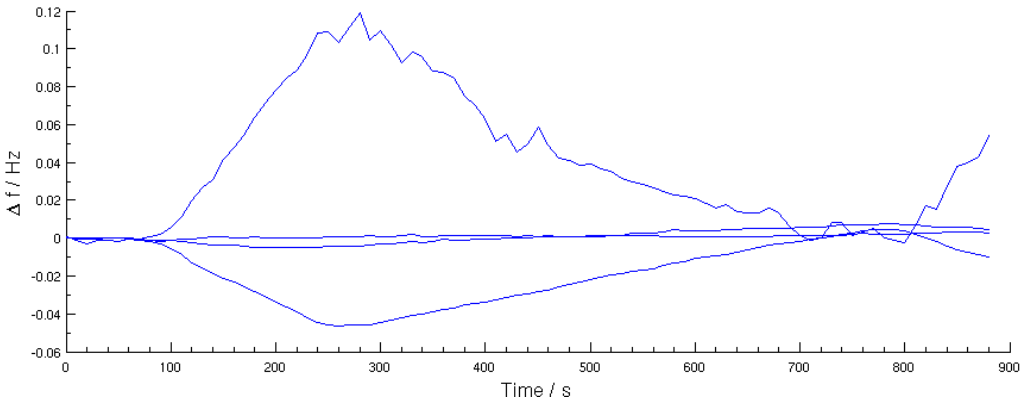

Figure 3.12: Functionality check of four bare quartz crystals.

Two crystals seem to be more stable, but with a frequency shift less than 0.12 Hz - all four crystals can be used for the experiment. The room temperature during this measurement (this applies for all QCM-D measurements) was at $(21.10 \pm .05)$°C, measured by a sensor in the device. Generally, the frequency shifts are divided by their overtone (to make them comparable), which is valid for all upcoming figures.

Figure 3.13 shows the frequency shift (7^{th} overtone) of the four crystals after the cellulose layers have been added. Now, the shifts are higher because cellulose is attached and the crystal is not in its designed state. The absolute frequencies can not be observed in the graphs (nor in the data files), but they were plotted on screen during the measurement. Of course, the frequency of the plain crystals was 5 MHz (plus the shift).

There is no data available of the swelling step itself, which leads to point four (heavy water exchange). In the range of 0 to 2100 seconds, figure 3.14 shows the 3^{rd} sample (the other three show similar behaviour) while rinsed with purified water. Heavy water was introduced into the flow module after 2100 seconds, resulting in a frequency drop of about 55 Hz and a dissipation increase of about $21 \cdot 10^{-6}$. A certain amount of water in the cellulose layer is replaced with heavy water - resulting in such a frequency drop. As the dissipation is quite high, the corresponding Sauerbrey mass is not valid because it underestimates the real

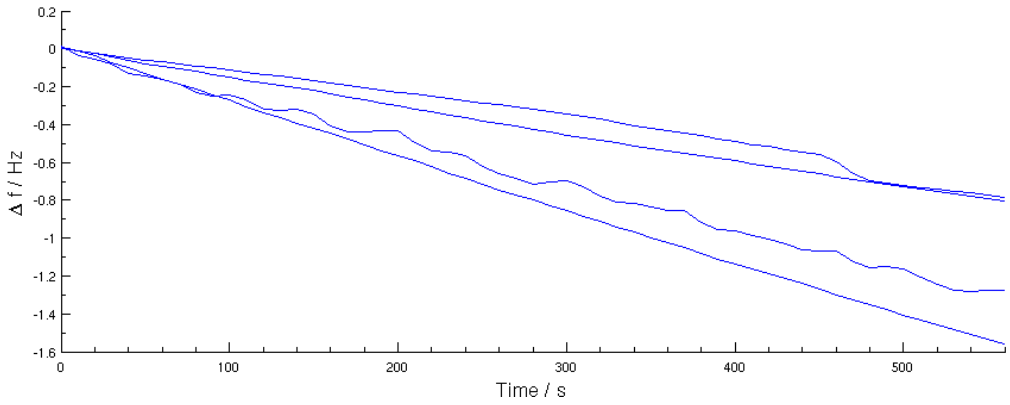

Figure 3.13: Functionality check of four quartz crystals - each coated with a cellulose layer.

mass difference. To calculate the water content in the cellulose layer, viscoelastic modelling would have to be done. Nevertheless, the Sauerbrey mass can serve as a lower limit. Applying Sauerbrey's equation to this 55 Hz frequency drop results in a mass change of about 1 μg. Now, one can estimate a lower limit for the water content in the cellulose layer, because the mass ratio between water and heavy water is known ($\approx 18 : 20 = 0.9$). The heavy water content is equal to the water content plus the mass difference. Applying this to the mass ratio results in a lower limit of the water content of 9 μg. At 4000 seconds, purified water was introduced again into the flow module. This brings back the frequency/dissipation shift to their initial state. There is a certain frequency increase (over the whole range) which could be caused by the water rinsing (small reduction of the attached layer). Overall, this measurement shows clearly, that there is an "exchangeable" amount of water in the cellulose layer. In case of a heavy water exchange, this shows steep frequency changes in time and is completely reversible. This circumstance is presented in another way through a so called "df-plot" (dissipation as a function of frequency). Df-plots can be quite useful to qualitatively compare different QCM-D experiments and give an impression of the "reaction path" of the adsoprtion/desorption occurring. These plots are time independent. Figure 3.15 shows such a plot for the heavy water exchange, one can see that starting and endpoints are nearly at the same spot - indicating reversibility. The arrow to the right side illustrates the change

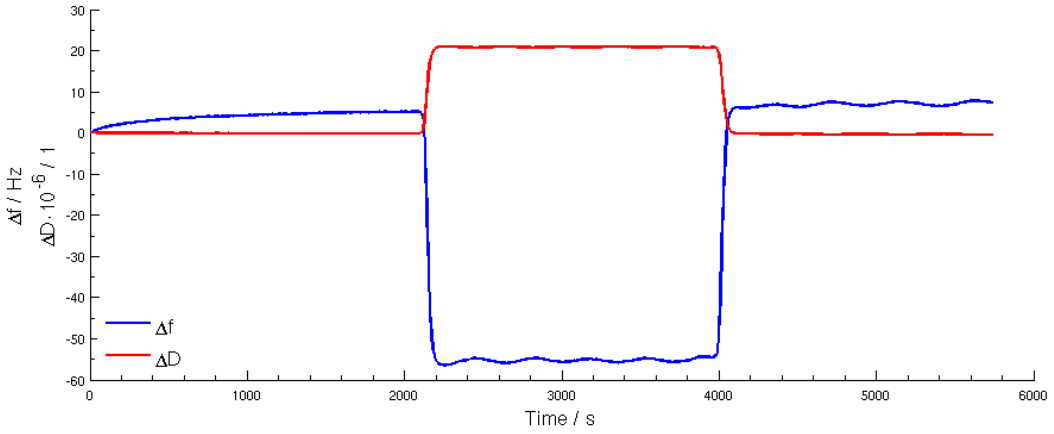

Figure 3.14: H_2O D_2O exchange of a cellulose coated quartz crystal (showing 5^{th} overtone of sample 3).

to heavy water, the other one the change back to water, both paths are similar.

Advancing to point 5, figure 3.16 shows the xylan adsorption of sample 2 and 4 (1 and 3 show similar behaviour and are therefore not drawn) using the 5^{th} overtone. Samples 1 and 2 have been rinsed with filtered xylan solution, samples 3 and 4 with unfiltered xylan solution. As a starting point, the samples have been equilibrated in the basic solution (alkaline aqueous solution). After that the xylan adsorption was started by introducing the xylan solutions into the flow module (at 650 seconds in figure 3.16). The frequencies (filtered and unfiltered) drop quickly about 25 Hz. This seems to be the exchange of the incorporated water with the heavier xylan solution. The dissipation increase of both samples (about $8 \cdot 10^{-6}$) is confirming this assumption. At 750 seconds, the frequency drop starts to saturate and goes down to about 45 Hz (at 2320 s) for the non filtered solution and to about 49 Hz (at 2320 s) for the filtered solution. In this range (750 to 2320 seconds) the actual xylan adsorption takes place. The filtering of the solutions shows an impact and results in a higher adsorption rate (about 3.5 Hz difference at 2320 seconds) and clearly less dissipation (a difference of $8 \cdot 10^{-6}$ at 2320 seconds). Moreover, the higher adsorbtion of the filtered solution is coupled with a lower dissipation increase during this process.

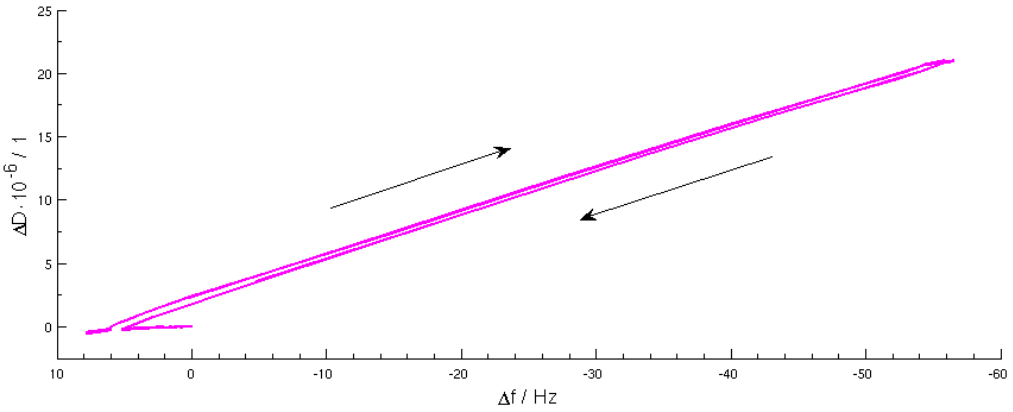

Figure 3.15: Df-plot of H_2O D_2O exchange of a cellulose coated quartz crystal (showing 5^{th} overtone of sample 3).

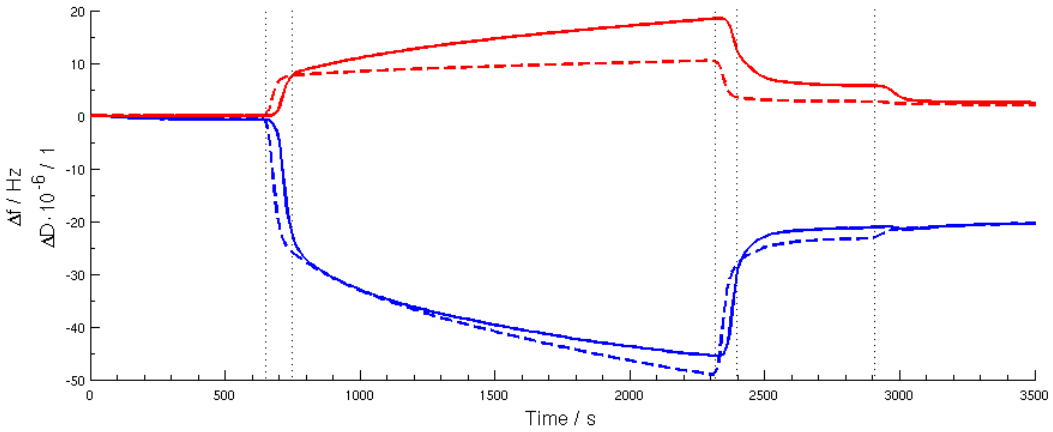

Figure 3.16: Frequency change (Δf in blue) and dissipation change (ΔD in red) during xylan adsorption on a cellulose coated quartz crystal using a filtered (dashed lines) and unfiltered xylan solution. The 5^{th} overtone of sample 2 and 4 is shown.

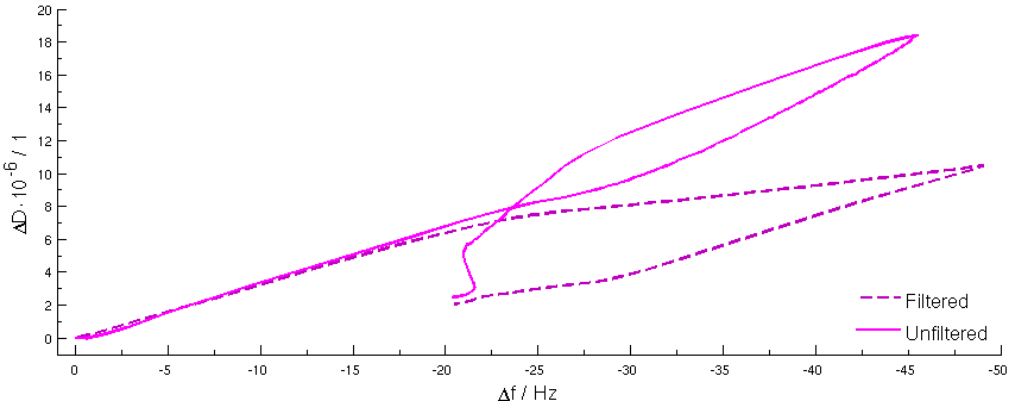

Figure 3.17: Df-plot of xylan adsorption on a cellulose coated quartz crystal (showing 5^{th} overtone of sample 2 and 4).

After the next rinsing step with the basic solution (starting at 2320 seconds), the unfiltered/filtered difference is reduced to about 2 Hz in frequency and $3 \cdot 10^{-6}$ in dissipation, but still is clearly observable. The second rinsing step (2320 to 2400 seconds) is basically the reverse of the first between 650 and 750 seconds. The xylan solution gets exchanged with basic solution again - resulting in a frequency increase in the range of 25 Hz (a bit less this time - not fully exchanged back). The last rinsing step with purified water shows an interesting detail (starting at 2900 seconds). The sample using the filtered solution experiences a barely observable dissipation drop while the frequency increases roughly 2 Hz. The other sample shows a dissipation drop of about $3 \cdot 10^{-6}$, with decreasing frequency in a barely noticeable manner. So, this rinsing step reduces mass at rather constant dissipation in the filtered case, while it changes rigidity at rather constant frequency change in the unfiltered case. These aspects can also be seen in the data of sample 1 & 3 and other overtones (not shown here). Figure 3.17 shows the df-plot of the data in figure 3.16. In comparison to figure 3.15 (heavy water exchange), starting and end point are not at the same spot. This is a result of a certain amount of xylan adsorbed persistently. In addition, filtered and unfiltered solutions show no difference at the starting/end points. This means that filtering the solution does not change the final amount of xylan adsorbed. Both processes go through

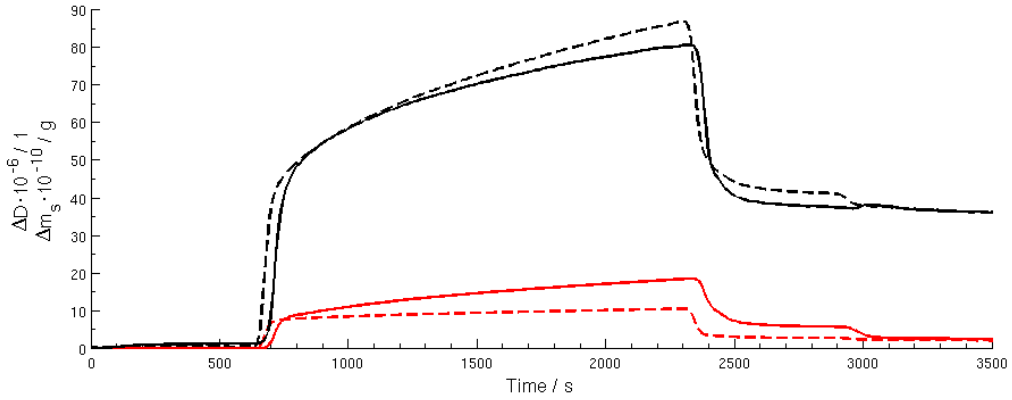

Figure 3.18: Dissipation (red) and Sauerbrey mass (black) during the xylan adsorption of sample 2 (filtered, dashed lines) and 4 (non-filtered). The Sauerbrey estimation of the mass change is only valid at low dissipation (about $2 \cdot 10^{-6}$ or less).

different dissipation/frequency paths in the intermediate area, pointing out the differences during adsorption described above. The last rinsing step with purified water is especially emphasised in this representation. Overall, xylan adsorption using the filtered solution seems to create a heavier and more rigid structure during adsorption. The difference persists during the basic solution rinsing step, but not the purified water rinsing step and has no influence on the final amount of xylan adsorbed. Because the dissipation is rather low (about $2.5 \cdot 10^{-6}$) after the last rinsing step, the frequency difference can be used to give a rough estimate of the adsorbed xylan mass per area. The estimation is drawn in figure 3.18, where, dissipation change of sample 2, 4 and the Sauerbrey mass are shown. The mass change is drawn over the full range, but only valid at low dissipation (which is the case at 3500 seconds). Table 3.3 lists the Sauerbrey masses calculated for the filtered and unfiltered case using all overtones and the fundamental oscillation. The frequency difference between 630 seconds and 3500 seconds was used for the calculation (see figure 3.18, the time axis is similar for all samples). One can see a clear decrease of mass with higher overtones. The fundamental and its high overtones are mainly used for viscoelastic modelling. If no modelling is applied, Q-Sense suggests the use of the third overtone. The xylan adsorption calculated with the third overtone

Table 3.3: Estimated xylan masses (m_s) adsorbed per sample surface (1 cm^2). The calculation has been done for all samples (m_{s1} to m_{s4}) and overtones (O) using the Sauerbrey equation.

	Filtered samples		Unfiltered samples	
O	m_{s1} / ng·cm^{-2}	m_{s2} / ng·cm^{-2}	m_{s3} / ng·cm^{-2}	m_{s4} / ng·cm^{-2}
1	357	431	491	415
3	339	378	462	387
5	315	360	455	345
7	287	343	441	343
9	279	324	432	333
11	264	308	-	330
13	247	455	390	-

gives a result of (391.5 ± 51.4) ng/cm^2. Using the atomic weight of the xylan stated in chapter 2.1.5, this is equivalent to $(4.35 \pm 0.57) \cdot 10^{-11}$ mol/cm^2.

3.3 Tensile tests of bound xylan adsorbed cellulose model films

In this experiment (introduced in chapter 2.4), three independent measurement series were done. For each one, forty cellulose model films were created with the method described in chapter 2.1.3. Table 3.4 gives a short overview of the different setups. First of all, the results of the calibration measurements (glued samples) will be discussed. Figure 3.19 shows the force depending on length variation in the "pressure stage" (while pressing the sample to the tape) of all calibration measurements (red ... series 1, green ... series 2, blue ... series 3). The length variation defines the distance of the rheometer bar (not the piston, because there are springs in it) to its position at maximum force. Negative forces are defined as tensile forces. To recap, the rheometer bar is moved at constant speed (0.02 mm / s) until the piston hits the sample. Then, the force is increased up to the maximum value of 40 N. Label E indicates calibration measurements using a reduced max force of 10 N, this can be useful to avoid

Table 3.4: Tensile test setup; each series is based on 40 cellulose model films. The sample count states the amount of samples successfully prepared (bound) for the tensile tests. The "filtered samples" row shows the amount of samples were xylan was adsorbed from a filtered solution.

Measurement parameters	Series 1	Series 2	Series 3
Sample count	17	18	14
Filtered samples	8	9	0
Calibration measurements	2	3	2
Water swelling duration	60 min	60 min	30 min
Duration of xylan adsorption	30 min	30 min	30 min
Water rinsing duration	-	-	30 min
Climate chamber storage	2 d	3 d	1 d
pH of xylan solution	8	7	8

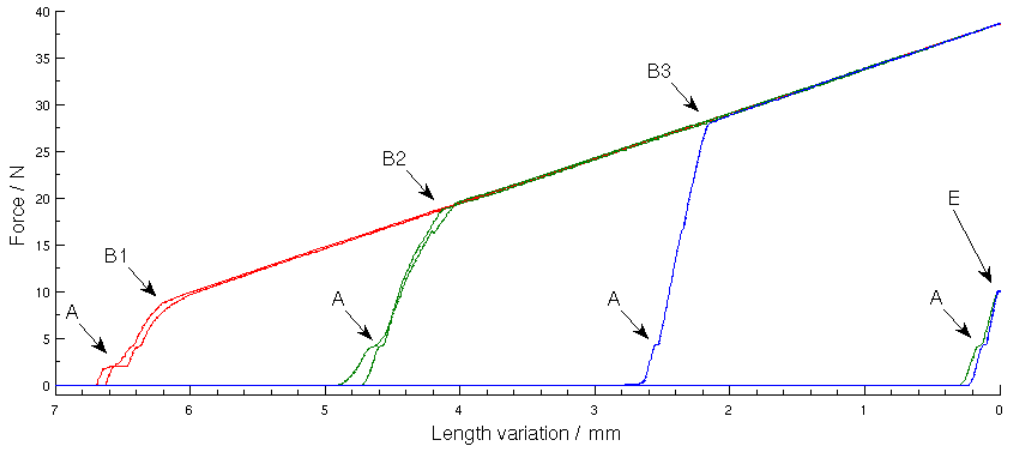

Figure 3.19: Pressure stage of calibration measurements - showing force dependent on length variation of the rheometer bar (red ... series 1, green ... series 2, blue ... series 3). Zero length variation defines the state of the bar at maximum force. Labels A to E are explained in the text.

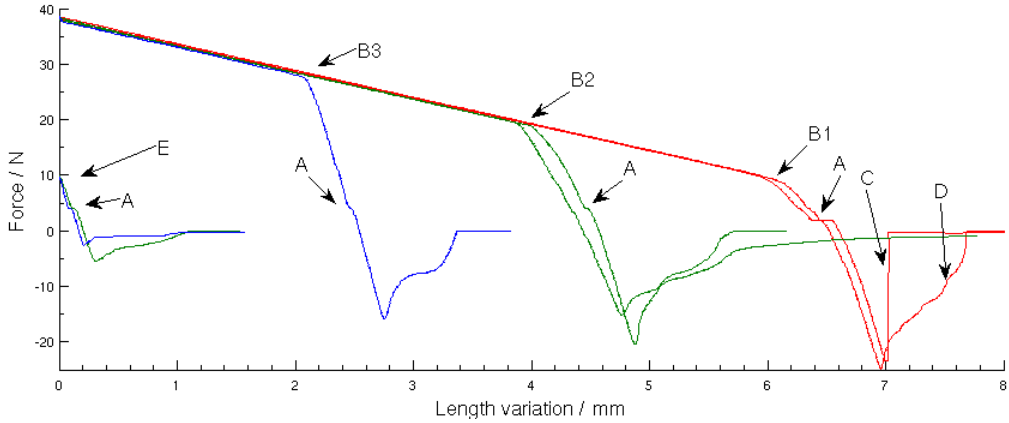

Figure 3.20: Loosening stage of calibration measurements - showing force dependent on length variation of the rheometer bar (red . . . series 1, green . . . series 2, blue . . . series 3). Negative forces are defined as tensile forces. Zero length variation defines the state of the bar at maximum force. Labels A to E are explained in the text.

premature fracturing. The differences in this figure are related to differently assembled rheometer pistons. When the piston is assembled tightly, the springs are pushed together with a certain force by default. In order to compress the springs further, this force has to be overcome first - resulting in the different behaviour in figure 3.19. The Arrows labelled B1 to B3 mark the spots where the springs start to compress further. Starting from there, the actual spring constant is drawn in the figure (from B to max force). In the region before (label A to B), there is a steeper force increase per length - showing the elasticity of the whole system (sample, piston, tape) without spring influence. The points labelled A show a reduced force increase right after hitting the sample. It is assumed that some part of rheometer is causing this, because it is recurring in all measurements and also showing in the "loosening stage" (decreasing of force from max value to zero). The first quadrant (positive force) of figure 3.20 represents this loosening stage, showing similar behaviour in comparison to the pressure stage. The actual measurement (tensile stage) happens at negative forces in figure 3.20, where the sample is pulled apart. As expected, the 10 N calibrations (label E) clearly show less binding strength. The first three rows of Table 3.5 list all these force minima of the tensile stage (the tensile

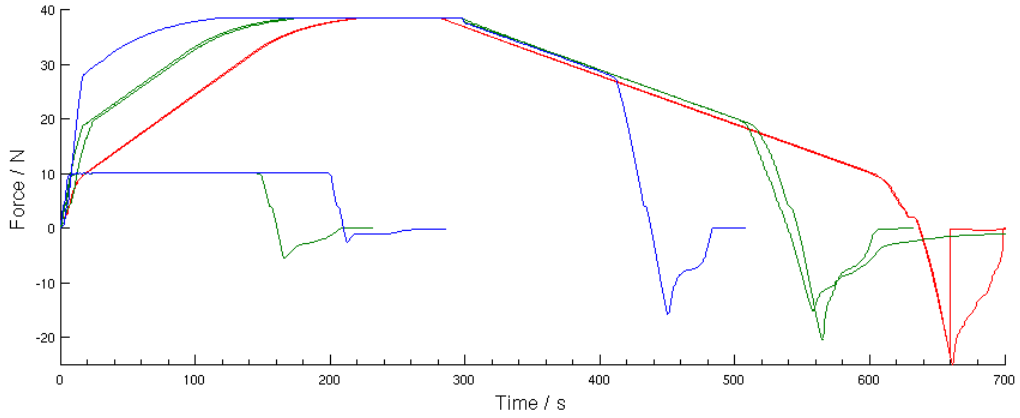

Figure 3.21: Force - time dependence of calibration measurements (red . . . series 1, green . . . series 2, blue . . . series 3).

force needed for tape separation). This acts as a framework for the actual measurements, because if a sample would sustain a force greater than those of the calibrations, the tape would separate instead of the sample. The labels C and D in figure 3.19 point out the difference of a "clean" separation (C) and a separation where the sample still had a connection to the tape after the initial break (D). This does not influence the results as long as this initial breaking point is distinguishable. To give another representation of the calibration data, figure 3.21 shows the tensile force depending on time of all three stages of the calibration measurements. Here, additionally to the aspects discussed above, one can see the total duration of such a measurement (about ten minutes) and the time the maximum force was held. Figure 3.22 shows the tensile stage from zero force to the first clear sign of separation (force minimum) of all calibration data. A linear fit was done for each line (because they have different length) and the fit coefficients have been averaged. The black line in figure 3.22 (labelled A) shows this averaged fit of the calibration measurements with the following coefficients: $k = (-61.3 \pm 9.4)$ N/mm and $d = (0.39 \pm 0.68)$ N. One can compare this to the calibration data of Rohm et al. [23] (dashed black line labelled B in figure 3.22) and note a slight variation of the coefficients: $k_{Rohm} = (-49.6 \pm 2.7)$ N/mm and $d_{Rohm} = (0.21 \pm 0.19)$ N. Because the same equipment was used

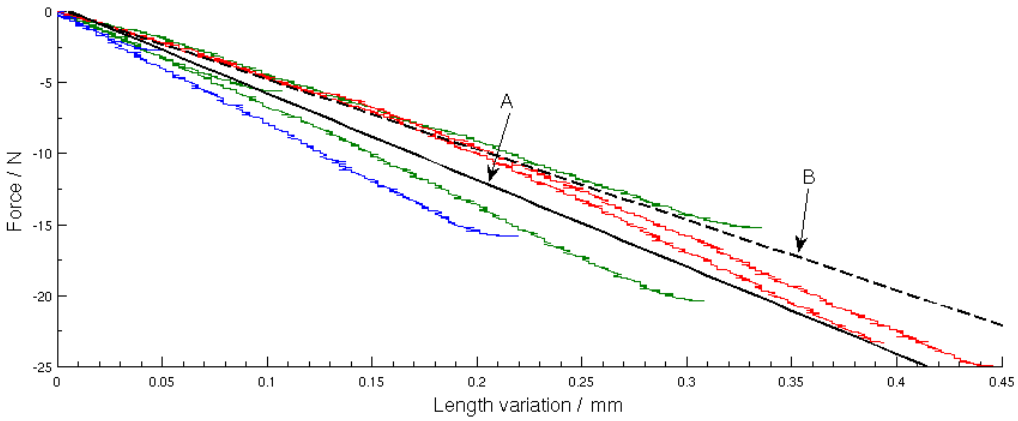

Figure 3.22: Force dependent on length variation of calibration measurements - showing tensile stage (cut off at force minima). The black line (label A) is a linear fit of the data, the dashed black line (labelled B) a comparison to the calibration fit done by Rohm et al. [23].

(including tape), it was expected to be in a similar range. But it is known that the properties of the tape change with time (storage), which explains the small differences. As a next point, the actual measurements of the first series will be discussed. As indicated in table 3.4, the samples were swelled in purified water for one hour, followed by a xylan adsoprtion step of 30 minutes. Half of the samples were adsorbed in a filtered xylan solution (see 2.1.5). The samples were divided into filtered and unfiltered ones. No water rinsing was done, so there still was a liquid layer of xylan solution on the surface before arranging the samples for drying. Neglecting the differences between the adsorption methods (flow system and a beaker on a magnetic stirrer), this situation is comparable to the position at 2320 seconds in figure 3.16 of chapter 3.2. There, the duration of the adsorption is about 28 minutes without rinsing. This means that there should be a higher xylan amount in the sample if no water rinsing step is done. Furthermore, the salt from the solution stays in the sample. Figure 3.23 shows the tensile force dependent on length variation of all tested samples in series 1. One can see from this overview, that the piston was reassembled one time (tighter) and a maximum force of 40 N was used for all samples. Some samples separated cleanly and sustained tensile forces up to about 19 N. Moreover,

Table 3.5: Results of all tensile tests; C1-C3 ... calibration 1 to 3; S1-S17 ... sample 1 to 17; F_{t,max,s_i} ... maximum tensile force obtained in series 1, 2 or 3; **bold values** ... samples adsorbed with filtered xylan solution; underlined values ... measured with reduced maximum force of 10 N in pressure stage.

Sample	F_{t,max,s_1} /N	F_{t,max,s_2} /N	F_{t,max,s_3} /N
C1	24.98	15.24	15.78
C2	23.32	20.37	-
C3	-	5.58	2.67
S1	**0.89**	0.00	0.00
S2	**6.52**	0.02	0.01
S3	**0.19**	0.00	0.01
S4	**1.26**	0.00	0.13
S5	**1.06**	0.01	0.00
S6	**8.26**	0.15	0.40
S7	**0.17**	0.21	0.01
S8	**10.82**	0.43	0.11
S9	1.17	**6.97**	0.10
S10	3.53	**2.12**	0.02
S11	0.27	**0.55**	0.02
S12	0.26	**0.92**	0.02
S13	10.83	**1.36**	0.00
S14	18.83	**0.28**	0.00
S15	-	**0.59**	-
S16	-	**0.15**	-
S17	-	**2.28**	-

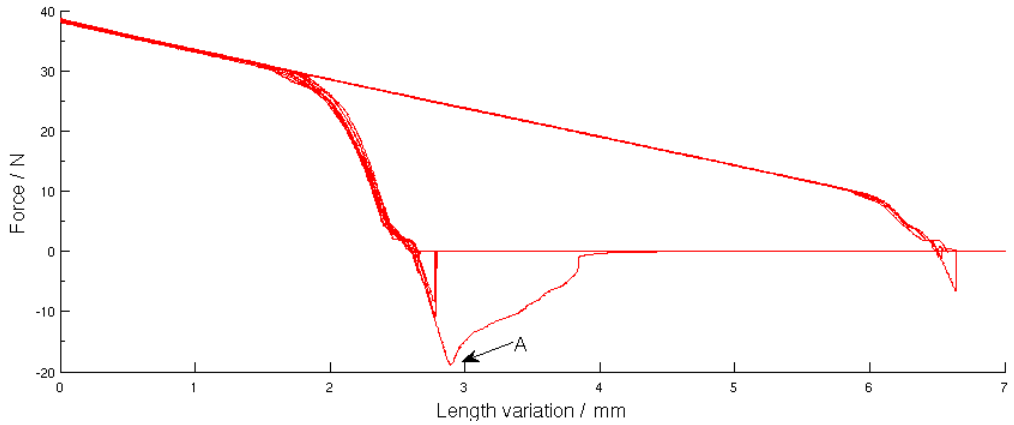

Figure 3.23: Results of series 1 - force dependent on length variation of the rheometer bar. Negative forces are defined as tensile forces. Zero length variation defines the state of the bar at maximum force. Label A indicates a tape ripoff.

arrow A indicates one sample that did not separate before the tape ripped off. Figure 3.24 shows the tensile stage only - a detail of Figure 3.23. Here, the unfiltered samples are coloured grey and the filtered ones red. One can see that both types sustained rather high tensile forces. The second column in table 3.5 lists the force minima of the tensile stage of these samples. Not all samples behaved similar, some broke before or did not show any binding strength at all. There are no significant differences between filtered and unfiltered samples. From Rohm et al. [23] it is known that the tensile force needed to separate 2x2 cm^2 pure cellulose model films is (1.86 ± 0.51) N. If assumed, that the tensile stress is evenly distributed over the surface, a quarter of this force would be expected for 1 cm^2 pure cellulose samples. Another difference to Rohm's measurements is the thickness of the samples. He spincoated four stacked layers using a 20 g/l TMSC-toluene solution - resulting in a (315 ± 75) nm film (measured by integrating the area under an infrared absorption-peak). If the layer thickness is linearly dependent on the concentration of the TMSC-toluene solution (which might not be the case), one could suppose, that the cellulose films in this work are 16 times thinner (about 20 nm). It is expected that this thickness is still large enough and should not make a difference in the

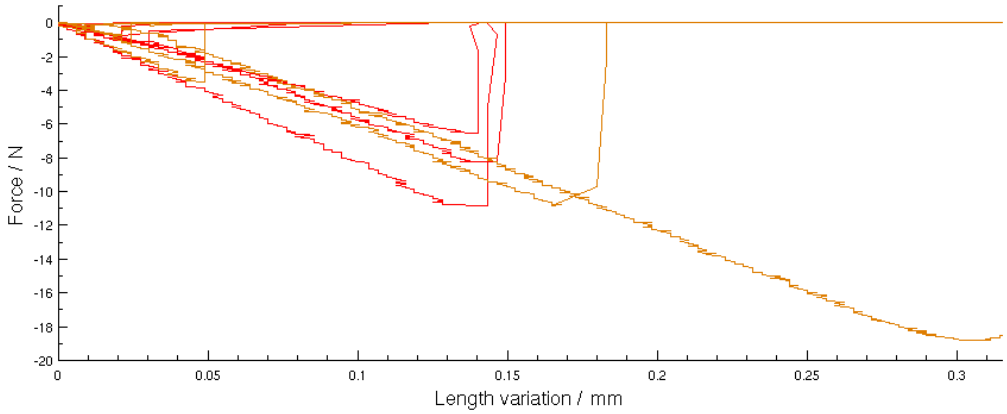

Figure 3.24: Detail of figure 3.23 (tensile stage). Red lines show filtered samples, brown lines unfiltered ones.

tests. With this in mind, the tensile forces observed in series 1 clearly show, that the adsorbed xylan in combination with salt heavily increases the binding strength of cellulose model films. In Rohm's measurements [23], (6.4 ± 1.5) N were averaged in 21 tests using 2x2 cm^2 spincoated xylan films with ionic (NaCl) swelling water. Considering sample size, the forces obtained here are much higher than expected.

The second series was done with some differences compared to the first one (noted in table 3.4). Again, 40 model films were created and processed, but no xylan solution was fabricated this time, instead the remaining solution from the first measurement (1 month storage) was used. A pH measurement revealed a drop from 8 to 7 and differences in opacity (compared to series 1) were distinguishable during the adsorption. Again, half of the samples were treated with the filtered xylan solution. Moreover, the samples were stored one day longer in the climate chamber before testing (3 days instead of 2) and purified water was used for swelling (instead of distilled water). Figure 3.25 shows the outcome of this experiment. Although similar findings to series 1 were expected, the tests showed different results. Using a maximum force of 40 N, the first seven filtered samples showed no binding strength. Because they seemed to be well bound before testing and did not break during handling, it

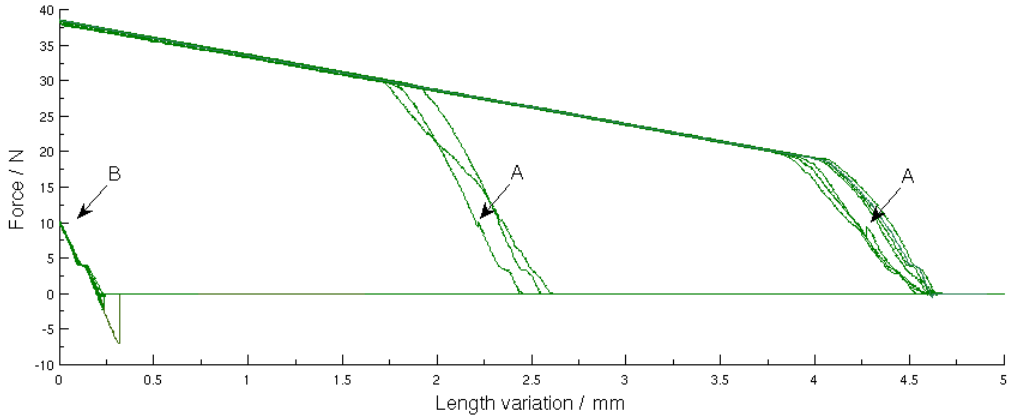

Figure 3.25: Results of series 2 - force dependent on length variation of the rheometer bar. Negative forces are defined as tensile forces. Zero length variation defines the state of the bar at maximum force. Labels A and B are explained in the text.

was assumed that they broke during the pressure phase. The arrows labelled A in figure 3.25 mark two spots with sudden force decreases were such early ruptures could be happening. Besides that, the calibration measurements were successful and did not indicate any problems with the rheometer. Based on this conclusion, the rheometer macro was edited, the maximum force was reduced to 10 N and the rest of the samples was tested with this configuration. Label B in figure 3.25 marks these measurements, where some samples showed better results. Figure 3.26 displays those tests in detail (tensile stage) and column 3 in table 3.5 lists the force minima. Apart from one sample sustaining a tensile force of about 7 N, the tests showed lower forces. No tape ripped off in this series. The possible alteration of the xylan solution through storage is seen as a main reason for the unstable results in this series. The longer climate chamber storage could also impact the binding strength to some extent.

The final series 3 was done to see if the amount of adsorbed xylan after a water rinsing step still increases the binding strength. To achieve this, the samples were swelled in purified water for 30 minutes, adsorbed in a xylan solution (fabricated one day before, no filtering) for 30 minutes and finally rinsed with purified water for 30 minutes before they were arranged into the

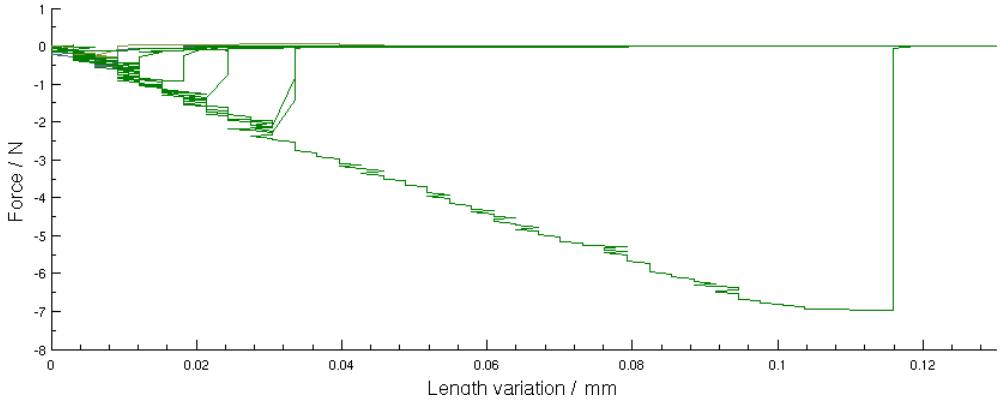

Figure 3.26: Detail of figure 3.25 (tensile stage) showing the measurements done with 10 N maximum force in pressure stage.

drier (see table 3.4). The rinsing step was basically a second water swelling step using a magnetic stirrer. The xylan adsorption after this procedure is comparable to the position at 3500 seconds in figure 3.16 of chapter 3.2. Only the xylan amount persisting the water rinsing step will stay in the samples. Furthermore, parts of the salt will be rinsed out before drying. Figure 3.27 displays the results of these measurements. Generally, the samples showed not enough binding strength to be measurable. An unusual high amount of samples did not survive the handling between drying and testing and broke prematurely. This already indicates low binding strength. The remaining fourteen samples showed could be mounted onto the rheometer socket without breaking. The calibration measurements did not show any inconsistency of the rheometer (see figure 3.21). After five samples showed no binding strength using 40 N force in pressure phase, the rest of the samples were examined with 10 N - without any improvement. Column three in table 3.5 lists all force minima obtained.

To conclude, it seems that with these smaller samples (1 cm^2 surface), tensile forces of a half Newton and lower are not easily measurable due to premature weakening of the bonds. Using the estimation done before (with the data from Rohm et al. [23]), pure bound cellulose model films would be in this range. A xylan adsorption in the range of 392 ± 123 ng/cm^2 is not enough to increase

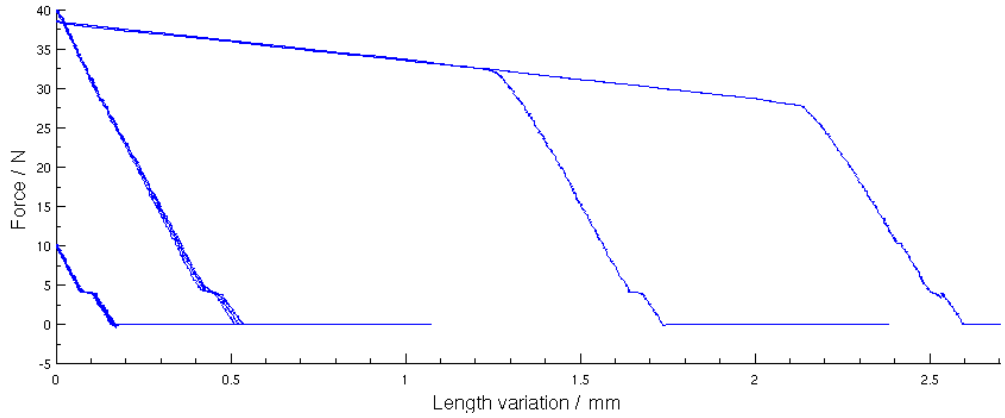

Figure 3.27: Results of series 3 - force dependent on length variation of the rheometer bar. Negative forces are defined as tensile forces. Zero length variation defines the state of the bar at maximum force.

the binding strength out of this region. However, an increased xylan adsorption incorporating salt is greatly improving the binding strength of such samples. This fits to the findings of Rohm et al. [23], but the resulting forces for samples adsorbed in an aqueous xylan solution with salt are much higher compared to Rohm's tests with spincoated films.

Finally, the calculation of bonding energies will be discussed. When integrating the force in respect to the length variation, an energy is obtained. This energy does not correspond to the actual bonding energy of the films, because the length variation is not the strain of the cellulose film. The system (rheometer, tape, etc.) has to be excluded by subtracting the "system energy" which is the area under the fit of the calibration curves. The resulting energy can be divided by the surface area of the samples to obtain the bonding energy per area. Such a bonding energy calculation out of tensile tests was done by S. Rohm et al. [23]. From there, it is known that this energy calculations have very large errors due to the inconsistency of the tape in the measurements. Nevertheless, the bonding energies have been evaluated. Only one measurement out of all series (sample 2 of series 1) showed a higher energy compared to the system energy, which is needed to obtain a non negative energy value. The

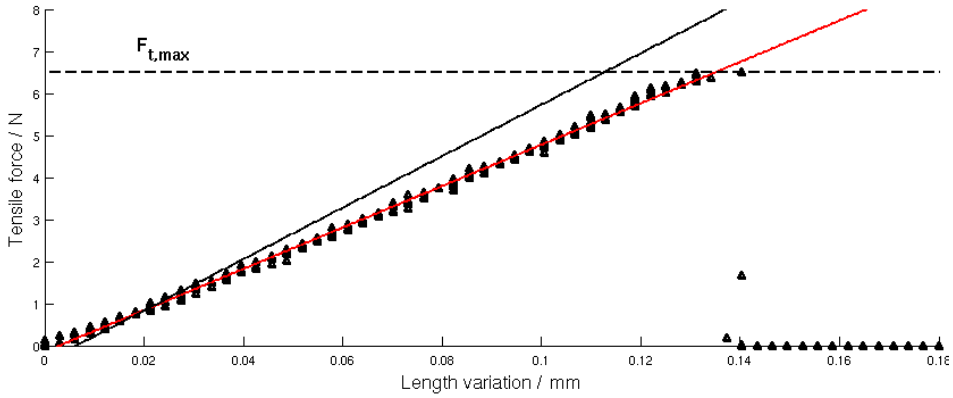

Figure 3.28: Linear fit of calibration measurements (black line), tensile strength data points of sample 2 out of series 1 and the linear fit of them up to maximum tensile force (red line).

bonding energy calculation of this sample is displayed graphically in figure 3.28. For convenience, linear fits have been used. The fit of the calibration curves is the black line with the following constants: $k = (61.3 \pm 9.4)$ N/mm and $d = (-0.39 \pm 0.68)$ N. The linear fit of the sample's data is drawn red and has following fit constants: $k_2 = 49.3$ N/mm and $d_2 = -0.14$ N. The maximum tensile force is indicated by the dashed line. Now, one needs to calculate the area under both curves up to their length variation values at maximum tensile force. Then, the system energy is subtracted from the overall energy and the result divided by the surface area, which gives the bonding energy per sample size. This calculation is also displayed quantitatively in equation 3.1 without the surface area division, where x is the length variation and x_{O_i} and x_{S_i} are the x values of the fits at zero and maximum tensile force. The resulting bonding energy per area for sample 2 is $(12 \pm 10) \cdot 10^{-22} \frac{kJ}{nm^2}$. The uncertainty is based on the error of the calibration fit (it has also been used relatively for sample 2) and the error of the sample surface (0.14 cm^2). If the variance of all series 1 samples would be used for the calculation, the error would be even higher and explain the occurrence of negative energy values. This makes clear that the evaluation of bonding energies based on the data obtained in these tests is

not reasonable.

$$E = \underbrace{\int_{x_{O_0}}^{x_{O_1}} \mathrm{d}x \ (k_2 x + d_2)}_{E_{Overall}} - \underbrace{\int_{x_{S_0}}^{x_{S_1}} \mathrm{d}x \ (kx + d)}_{E_{System}} \approx \frac{1}{2}(k_2 x_{O_1}^2 - k x_{S_1}^2) \tag{3.1}$$

4 Conclusions and outlook

- Using infrared spectroscopy in transmission, a range of important cellulose absorption bands between 850 to 1400 wavenumbers were successfully identified in bound and unbound samples. Their band minima were directly compared, which revealed no significant differences. The spectra of the bound samples generally showed more noise and interference effects, which made the comparison difficult. This is most likely caused by their stronger layered structure. The reflection spectra are affected by these aspects more severely and did not show viable results. In general, the experiment did not lead to direct references on bonding mechanisms of cellulose model films. However, if the side effects are further reduced (e. g. by the use of single side polished wavers, reducing the air gap between wafers in background measurements, applying background corrections or a better mirror adjustment) the method can be feasible (in transmission) for future experiments comparing bound model films with different parameters.
- In wet state, cellulose model films have a high water content, it has been shown that some of this water can be exchanged reversibly with heavy water. A lower limit of the water content for such 1 cm^2 films was calculated, resulting in 9 μg. When rinsed with an aqueous alkaline xylan solution (pH 8, 0.5 g/l) including 1 mMol NaCl, these films show a mass increase which persists at least thirty minutes of water rinsing. This form of xylan adsorption showed an addition of (391.5 ± 51.4) ng/cm^2 mass in thirty minutes (not saturated). The use of a filtered xylan solution resulted in a lower dissipation increase during adsorption, but had no significant impact on the final amount adsorbed. For future measurements, the

know-how of this experiment could be used to directly compare the xylan adsorption behaviour on cellulose model films using different solution parameters (e. g. modified pH values or ionic contents), different xylans or other adsorbates. Furthermore, viscoelastic modelling can be done to obtain better estimations on the adsorbed masses.

- Compared to plain cellulose model films, tensile tests of xylan adsorbed films showed a heavy increase in bonding strength when they were bound directly out of the xylan solution (no water rinsing). In this case the maximum tensile forces of fourteen 1 cm^2 samples were distributed in a range of 19 N. With a water rinsing step after the xylan adsorption, non of fourteen samples showed higher tensile forces than 0.4 N, which is in the range of pure cellulose samples. The filtering of the solution showed no influence. This experiment demonstrated that a high enough xylan adsorbtion in presence of ionic compounds drastically improves the bonding strength of cellulose model films. It emphasises the importance of Coulomb interactions as a bonding mechanism, which could play a more important role than currently assumed. A critical part in this measurements was the tape and its inconsistency. For further experiments, a better mounting mechanism for the bound samples would reduce the variance and make bonding energy calculations reasonable. Such a mechanism would have to be independent (no connections, tubes etc.) and satisfy a constant influence to the rheometer bar (over several measurements) which can be subtracted from the obtained data. This is a difficult task, because mechanical stress to the bound samples should be minimised before the measurements. A simpler improvement could be a thinner and more rigid tape with preferably stable elastic properties.

Bibliography

[1] S. Blundell. *Concepts in thermal physics*. Oxford: Oxford University Press, 2006. ISBN: 978-0-19-856769-1.

[2] J. C. Brice. "Crystals for quartz resonators". In: *Rev. Mod. Phys.* 57 (1 Jan. 1985), pp. 105–146. DOI: 10.1103/RevModPhys.57.105.

[3] W. Briese and B. Neubig. *The crystal cookbook*. Vol. 1. Franzis-Verlag, 1997. ISBN: 978-3-7723-5853-5.

[4] P. Bruice. *Organic chemistry*. Pearson/Prentice Hall, 2004. ISBN: 978-0-13-140748-0.

[5] W. Demtröder. *Atome, Moleküle und Festkörper*. Vol. 3. Experimentalphysik. Berlin Heidelberg: Springer-Verlag, 2010. ISBN: 978-3-642-03910-2.

[6] M. Djak. "Untersuchung von Cellulose-Hemicellulose Filmen auf Si/SiO_2 Substraten mittels polarisationsmodulierter Fourier-Transformations-Infrarotspektroskopie". MA thesis. Graz University of Technology, 2011.

[7] M. Djak et al. "Thickness dependence of reflection – absorption infrared spectra of supported thin polymer films". In: *Macromolecules* 44.7 (2011), pp. 1775–1778. DOI: 10.1021/ma102905v.

[8] C. Geffroy et al. "Kinetics of adsorption of polyvinylamine onto cellulose". In: *Colloids and Surfaces A: Physicochemical and Engineering Aspects* 172.1–3 (2000), pp. 47–56. ISSN: 0927-7757. DOI: 10.1016/S0927-7757(00)00499-4.

[9] E. Gilli. "Infrarot-spektroskopische Untersuchungen der chemischen Oberflächeneigenschaften von Cellulosefasern". MA thesis. Graz University of Technology, 2008.

[10] P. R. Griffiths and J. A. de Haseth. *Fourier transform infrared spectrometry*. 2nd ed. WILEY, Apr. 2007. ISBN: 978-0-471-19404-0.

[11] F. Hook et al. "The dissipative QCM-D technique: interfacial phenomena and sensor applications for proteins, biomembranes, living cells and polymers". In: *Frequency and Time Forum, 1999 and the IEEE International Frequency Control Symposium, 1999., Proceedings of the 1999 Joint Meeting of the European*. Vol. 2. 1999, pp. 966–972. DOI: 10.1109/FREQ.1999.841467.

[12] D. Klemm et al. *Comprehensive cellulose chemistry: fundamentals and analytical methods*. Vol. 1. WILEY-VCH, 1998. ISBN: 978-3-527-29413-9.

[13] D. Klemm et al. "Cellulose: fascinating biopolymer and sustainable raw material". In: *ChemInform* 36.36 (2005), pp. 3358–3393. ISSN: 1522-2667. DOI: 10.1002/chin.200536238.

[14] T. Kondo and C. Sawatari. "A Fourier transform infra-red spectroscopic analysis of the character of hydrogen bonds in amorphous cellulose". In: *Polymer* 37.3 (1996), pp. 393–399. ISSN: 0032-3861. DOI: 10.1016/0032-3861(96)82908-9.

[15] H. Kono and Y. Numata. "Two-dimensional spin-exchange solid-state NMR study of the crystal structure of cellulose II". In: *Polymer* 45.13 (2004), pp. 4541–4547. ISSN: 0032-3861. DOI: 10.1016/j.polymer.2004.04.025.

[16] E. Kontturi, T. Tammelin, and M. Osterberg. "Cellulose-model films and the fundamental approach". In: *Chem. Soc. Rev.* 35 (12 2006), pp. 1287–1304. DOI: 10.1039/B601872F.

[17] E. Kontturi, P. C. Thüne, and J. W. Niemantsverdriet. "Novel method for preparing cellulose model surfaces by spin coating". In: *Polymer* 44.13 (2003), pp. 3621–3625. ISSN: 0032-3861. DOI: 10.1016/S0032-3861(03)00283-0.

[18] T. Lindström, T. Larsson, and L. Wågberg. "On the nature of joint strength in paper - a review of dry and wet strength resins used in paper manufacturing". In: *13th Fundamental Research Symposium*. The Pulp and Paper Fundamental Research Society. Cambridge, 2005, pp. 457–562. ISBN: 978-0-9545272-3-5.

[19] C. K. O'Sullivan and G. G. Guilbault. "Commercial quartz crystal microbalances – theory and applications". In: *Biosensors and Bioelectronics* 14.8–9 (1999), pp. 663–670. ISSN: 0956-5663. DOI: 10.1016/S0956-5663(99)00040-8.

[20] Q-Sense. *Q-Sense E4 product brochure*. 2014 (accessed March 28). URL: http://www.q-sense.com/file/q-sense-e4-auto.pdf.

[21] Q-Sense. *Q-Sense sensor product brochure*. 2014 (accessed March 28). URL: http://www.q-sense.com/file/q-sense-sensors.pdf.

[22] S. Rohm. "Thin cellulose films as model systems for paper-fibres". MA thesis. Graz University of Technology, 2013.

[23] S. Rohm et al. "Thin cellulose films as a model system for paper fibre bonds". In: *Cellulose* 21.1 (2014), pp. 237–249. ISSN: 0969-0239.

[24] G. Sauerbrey. "Verwendung von Schwingquarzen zur Wägung dünner Schichten und zur Mikrowägung". German. In: *Zeitschrift für Physik* 155.2 (1959), pp. 206–222. ISSN: 0044-3328. DOI: 10.1007/BF01337937.

[25] M. Schaub et al. "Ultrathin films of cellulose on silicon wafers". In: *Advanced Materials* 5.12 (1993), pp. 919–922. ISSN: 1521-4095. DOI: 10.1002/adma.19930051209.

[26] R. Schennach et al. "A new method for performing polarization modulation infrared reflection-adsorption spectroscopy of surfaces". In: *Appl. Spectrosc.* 63.3 (Mar. 2009), pp. 369–372.

[27] H. Sixta. *Handbook of pulp*. Vol. 1. Weinheim Chichester: Wiley-VCH John Wiley, distributor, 2006. ISBN: 978-3-527-30999-3.

[28] C. Steinem, A. Janshoff, and O. S. Wolfbeis, eds. *Piezoelectric sensors*. Vol. 5. Springer Series on Chemical Sensors and Biosensors. Springer, 2006. ISBN: 978-3-540-36567-9.

[29] P. Zugenmaier. *Crystalline cellulose and cellulose derivatives characterization and structures*. Springer Series in Wood Science. Berlin New York: Springer, 2008. ISBN: 978-3-540-73933-3.